

PATTERN FORMATION IN DRYING DROPS OF COLLOIDAL SOLUTIONS

by

Ziye Xiong

B.A, Hubei University of Technology, 2011

Submitted to the Graduate Faculty of
Swanson School of Engineering in partial fulfillment
of the requirements for the degree of
Master of Science

University of Pittsburgh

2013

UNIVERSITY OF PITTSBURGH
SWANSON SCHOOL OF ENGINEERING

This thesis was presented

by

Ziye Xiong

It was defended on

March 21st, 2013

and approved by

Jung-Kun Lee, PhD, Assistant Professor

Department of Mechanical Engineering and Materials Science

Anthony J. DeArdo, PhD, Professor,

Department of Mechanical Engineering and Materials Science

John A. Barnard, PhD, Professor

Department of Mechanical Engineering and Materials Science

Thesis Advisor: John A. Barnard, PhD, Professor

Copyright © by Ziyè Xiong

2013

PATTERN FORMATION IN DRYING DROPS OF COLLIDAL SOLUTIONS

Ziye Xiong, M.S.

University of Pittsburgh, 2013

The deposited residue from evaporated drops of colloidal solutions can exhibit a wide variety of interesting and reproducible patterns. A familiar example is the ring-like residue associated with the "coffee ring effect"[1]. This phenomenon was first explained by Deegan, *et al* as due to outward (radial) flows introduced by evaporation driving the suspended particles to the self-pinned edge, creating a "coffee ring" structure at the drop perimeter. This behavior has drawn the attention of a number of other researchers interested in its applications and relevance to industrial processes and technology (i.e. printing, coating, and medical diagnostics). Recently, certain diseases have been associated with specific patterns in dried drops of blood serum [2]. Important studies on the key mechanisms of the process (e.g. evaporation kinetics, internal flow motions, triple line dynamics role in evaporative self-assembly phenomena) have also appeared. During the evaporation of colloidal sessile droplets, capillary and Marangoni flow and Van der Waals forces work together. With so many factors effecting pattern formation, small changes in solution composition can lead to significant changes in the resulting patterns. In this research project, model solutions are made using a base lysozyme protein aqueous solution mixed with aqueous sodium chloride solutions of various concentrations. Droplet patterns from these colloidal solutions are examined by atomic force microscope and digital optical microscope. The sodium chloride concentration dependent patterns are analyzed and the temporal stability of these patterns in air at room temperature is monitored over several months.

TABLE OF CONTENTS

ACKNOWLEDGEMENT.....	XIV
1.0 INTRODUCTION.....	1
2.0 THEORY	5
2.1 WETTING.....	5
2.1.1 Surface Tension.....	5
2.1.2 Young’s Equation	6
2.2 DROPLET EVAPORATION.....	7
2.2.1 Evaporation Model.....	7
2.2.2 Evaporation Rate.....	8
2.3 DENDRITIC GROWTH OF CRYSTALS.....	9
3.0 REVIEW OF THE LITERATURE.....	11
3.1 PATTERN FORMATION IN EVAPORATING DROPS.....	11
3.1.1 Evaporative Dynamics and General Pattern Formation	12
3.1.2 Pattern Formation in Micro-scale Droplets	14
3.2 PATTERN FORMATION OF BIOFLUID DROPLETS.....	14
3.3 LYSOZYME	19
3.3.1 Lysozyme properties.....	19
3.3.2 Electrical properties	20

3.3.3	Transport Properties	20
3.3.4	Aggregation and crystallization	21
3.4	PHASE TRANSITIONS IN EVAPORATING DROPLETS	23
3.5	EFFECT OF SALT CONCENTRATION ON PROTEIN PATTERN FORMATION.....	24
4.0	RESEARCH DESCRIPTION.....	25
4.1	HYPOTHESIS	25
4.2	OBJECTIVES	25
5.0	EXPERIMENTAL DETAILS	27
5.1	SOLUTION PREPARATION.....	27
5.2	SUBSTRATES AND DEPOSITION TECHNIQUES.....	28
5.3	OPTICAL MICROSCOPY	29
5.4	ATOMIC FORCE MICROSCOPY.....	30
5.5	EXPERIMENTAL UNCERTAINTIES	33
6.0	RESULTS AND DISCUSSION	34
6.1	RESULTS FROM L100 TO LN100.....	34
6.1.1	L100.....	34
6.1.2	LN001.....	36
6.1.3	LN005.....	38
6.1.4	LN010.....	40
6.1.5	LN025.....	43
6.1.6	LN050.....	46
6.1.7	LN100.....	48
6.2	AVERAGE VALUES OF W/D AND H_R/H_C	49

6.3	EFFECT OF SALT CONCENTRATION ON PATTERN FORMATION.	50
6.3.1	The morphology of ring of deposits	51
6.3.2	Dendrites in the deposits of LN050 and LN100	52
6.3.3	Pore-like structures on the rings	54
7.0	CONCLUSION.....	56
7.1	MORPHOLOGICAL PATTERNS.....	56
7.2	TOPOGRAPHICAL FEATURES	57
7.3	TIME DEPENDENCE	58
	BIBLIOGRAPHY	59

LIST OF TABLES

Table 3.3.1 Average concentrations of some important proteins and ions in human tears.	18
Table 3.3.2 Properties of lysozyme.....	20
Table 5.1. Summary of solutions studied.....	27
Table 6.1. Average values of w/D and h_r/h_c	50

LIST OF FIGURES

Figure 2.1 .Illustration of interfacial tensions and contact angle of a liquid droplet wetted to a solid surface.	6
Figure 2.2. Geometry of the model system.....	7
Figure 2.3. Morphology of dendrite growth with increasing relative initial impurity contents from a to e, which show secondary and tertiary branches. The black lines show the salt distribution and the gray region are the impurity transferred to a different phase [19].	10
Figure 3.1.Schematic of outward flow of a drying droplet and evaporative flux (J) [19].	12
Figure 3.2. The morphological features of dried drops of serum in norm and different diseases: (a) healthy individual (control group); and patients with (b) breast cancer; (c) lung cancer; (d) paraproteinemia; (e) in-time delivery; (f) premature delivery; (g) threatened abortion in different periods; (h) hepatitis [43].....	16
Figure 3.3. (a) and (c) are dried droplets of blood from healthy individuals with different ages, while (b) and (d) are person with anaemia and hyperlipidaemia [2]	17
Figure 3.4. Postulated phase diagram for globular proteins. (a) normal solubility (b) retrograde solubility. Zone I is region for protein crystallization. Zone II: liquid-liquid phase separation. Zone III is a region of gelation [64].....	22
Figure 5.1. Reflection optical microscopy images illustrating typical droplet sizes produced by aerosol deposition of lysozyme solutions a), b) $\rho = 1.0$ g/100mL, c) 1.0g/100mL containing 0.5g/100mL NaCl, d) 1.0g/100mL containing 0.25g/100mL NaCl. a) $\times 100$; b)c,d) $\times 500$	29
Figure 5.2. Basic setup schematic for SPM system.....	32
Figure 6.1. Representative image of a lysozyme drop deposit with $\rho = 1.0$ g/100 mL. (a) Optical microscopy image; (b) 2-D AFM topographic map with 50 μ m X 50 μ m area; (c) 3-D view of AFM topography data; (d) Cross-sectional height profile.....	35

Figure 6.2. Representative image of a lysozyme-based drop deposit containing 0.01 wt% NaCl. a) Optical microscopy image; b) 2-D AFM topographic map with 50 μ m X 50 μ m area; c) 3-D view of AFM topography data; d) Cross-sectional height profile. 37

Figure 6.3. Representative image of a lysozyme-based drop deposit containing 0.05 wt% NaCl. a) Optical microscopy image; b) 2-D AFM topographic map with 50 μ m X 50 μ m area; c) 3-D view of AFM topography data; (d) Cross-sectional height profile. 38

Figure 6.4. e) Detail view of deposit interior, AFM topographic map (10 μ m X 10 μ m); f) detailed view of peripheral ring, AFM topographic map (10 μ m X 10 μ m). 39

Figure 6.5. Representative images of pattern 1 of the deposit from the standard lysozyme solution with a NaCl solution concentration of 0.10 wt%. a) Optical microscopy image; b) 2-D AFM topographic maps (50 μ m X 50 μ m); c) 3-D view of AFM topography data; d) Cross-sectional height profiles. 40

Figure 6.6. Representative images of pattern 2 of the deposit from the standard lysozyme solution with a NaCl solution concentration of 0.10 wt% with a diameter > 30 μ m. a) Optical microscopy image; b) 2-D AFM topographic maps (50 μ m X 50 μ m); c) 3-D view of AFM topography data; d) Cross-sectional height profiles. 42

Figure 6.7. Optical image of a larger diameter (~ 50 μ m) lysozyme deposit containing 0.1% NaCl. 42

Figure 6.8. Representative image of a lysozyme-based drop deposit containing 0.25 wt% NaCl. a) Optical microscopy image; b) 2-D AFM topographic map with 50 μ m X 50 μ m area; c) 3-D view of AFM topography data; d) Cross-sectional height profile. 43

Figure 6.9. e) Detail view of deposit interior, AFM topographic map (10 μ m X 10 μ m); f) Detailed view of peripheral ring, AFM topographic map (10 μ m X 10 μ m). 44

Figure 6.10. a) b) c) d) represent the same deposit one week after the sample (LN025) is made. 45

Figure 6.11. Representative images of a lysozyme-based drop deposit containing 0.50wt% NaCl. a) Optical microscopy image; b) 2-D view AFM topographic map (50 μ m X 50 μ m); c) 3-D view of AFM topography data; d) Cross-sectional height profile. 46

Figure 6.12. Detailed view of deposit interior indicated by the blue square in figure 6.12 (b), AFM topographic map (10 μ m X 10 μ m); f) 3-D view of AFM topography data, (10 μ m X 10 μ m); g) Optical image of the same deposit one week after the sample is made. 47

Figure 6.13. Representative images of a lysozyme-based drop deposit containing 1.0 wt% NaCl. a), e) Optical microscopy images; b) 2-D view AFM topographic map (50 μ m X 50 μ m); c) 3-D view of AFM topography data, (50 μ m X 50 μ m); d) Cross-sectional height profile through the center. (blue line in (b)); f) Central crystal height profile (marked with the red line in (b)). 48

Figure 6.14. Plot of $-\ln(w/D)$ (relative width of Region I (ring)), vs. $\ln \phi N$, the relative salt concentration. Inset in the graph are images showing Regions I for drops containing 0.01, 0.05, 0.25, 0.50, and 1.00 wt% NaCl. 52

Figure 6.15. Detail images taken from deposits containing (a) 0.5% NaCl (b) 1% NaCl, AFM topographic map ($10\mu\text{m} \times 10\mu\text{m}$). 53

Figure 6.16. Detail images taken from deposits containing (a) 0.05% NaCl (b) 0.25% NaCl, AFM topographic map ($10\mu\text{m} \times 10\mu\text{m}$)..... 54

Figure 6.17. SEM image of the central region (Region III) of a lysozyme-based deposit containing 0.01wt% NaCl[37]. 55

NOMENCLATURE

A	Surface area, m^2
C	Vapor concentration
C_p	Heat capacity, $4180 \text{ (J kg}^{-1} \text{ K}^{-1}\text{)}$
C_v	Saturation vapor concentration
C_∞	Ambient vapor concentration
$C_{s,s}$	Density of the solid salt
C_s	Instantaneous density of salt
C_{sat}	Saturation concentration of the solution,
D	Droplet diameter
D_i	Inner deposit diameter
D_L	Diffusion coefficient of lysozyme, $D_L=1 \times 10^{-10} \text{ m}^2/\text{s}$.
D_v	Vapor diffusivity, water, $21.6 \times 10^{-6} \times (1+0.0071T)$
G	Gibbs free energy
g	Acceleration due to gravity, 9.81 m/s^2
h	Droplet height
J	Evaporative flux
L	Characteristic length
M_w	Molar mass of water, 18.0152 g/mol
n	Number of molecules in the system
p	Pressure
P_{VS}	Saturation water vapor pressure $P_{VS}=610.7 \times 10^7 \cdot 5T^{237.3+T}$
R	Droplet radius, m

R_g	Ideal gas constant, 8.314 J/mol·K
R_p	Particle radius, lysozyme, 2 nm
t	Time, s
T	Temperature, K
u	Radial flow velocity, m/s
U	Potential energy, J
V	Volume, m ³
V_1	Volume of single lysozyme molecule, 21.2 nm ³
V_L	Liquid drop volume
w	Width of the deposit ring

Greek Symbols

γ	Surface tension, N/m
η	Viscosity
θ	Contact angle
θ_0	Initial contact angle
θ_D	Deposit contact angle
κ	Thermal conductivity, water, 0.607 (W m ⁻¹ K ⁻¹)
μ	Dynamic viscosity, $(-0.0026T^3+0.5874T^2-47.598T+1763.4) \times 10^6$ Pa s
φ	Solute concentration
φ_L	Lysozyme solution concentration
φ_N	NaCl solution concentration
Φ_N	Relative NaCl concentration

ACKNOWLEDGEMENT

I would like to gratefully and sincerely thank my advisor, Dr. John A. Barnard for his great guidance and generous support throughout my research. I would have never accomplished this research without his help and support.

My thanks also go to my committee members: Dr, Anthony J. DeArdo, Dr Jung-Kun Lee and Dr John A. Barnard. I truly appreciate their time and help for making this thesis better. Also, I would like to thank my lab partner, Heather Meloy Gorr and Josh Zueger for their valuable advices.

Last, I would like thank my family and friends' encouragement.

1.0 INTRODUCTION

Solute self-organization during the evaporation of a colloidal droplet is a common phenomenon in daily life. For example, the well-known “coffee ring effect” describes the pattern formation leading to a coffee ring stain. Particles in a drying droplet are driven to the edge and form a perimeter ring by outward flows. Pattern formation in a drying sessile droplet is a relatively simple and repeatable experiment to carry out but the final patterns depend sensitively on the interplay of complex physical mechanisms. This complexity has attracted the attention of a number of research groups in the last ten years. As Deegan has described, capillary flow can develop a contact-line deposit by forcing the suspended particles in the solution to the edge of a drying drop. In his simple colloidal droplet model system, the shape of the deposit can be predicted and controlled [1]. In contrast to capillary flow, Marangoni flow, an inward radial flow caused by convective heat transfer, recirculates the particles along the droplet surface and draws them to the center of the drop, which finally forms an axisymmetric pattern. Deposition patterns are also influenced by contact line depinning and particle concentration effects [3]. Interactions among solute(s), solvent and substrate also play a role in the drying system in addition to the flows just described. Phase transitions can be triggered during evaporation of sessile droplets because of the gradual depletion of solvents. Glass transitions and gelation have been observed in colloidal desiccating drops of polymer solutions [4] and blood [5]. Associated with these

interesting behaviors in drying drops are a range of technological applications of solute self-organization in a number of fields, such as fabrication of polymer films [6], drug screening [7], DNA microarray printing [8], microfluidics [9] and disease detection and diagnosis [2].

Drying sessile droplets of human biofluids such as blood, tears, and saliva are non-Newtonian fluids with multiple-components including proteins, electrolytes, lipids and electrolytes. The particle-particle and particle-substrate interactions and transport mechanisms become more complicated in biofluids, which can lead to highly complex patterns. Several studies have explored pattern formation in biofluids in recent years. Brutin and his co-workers examined pattern formation in drying drops of blood for a healthy human as well as for anaemic and hyperlipidaemic patients. Distinguishable patterns were observed with differences in crack patterns and corona thickness for different diseases [2]. These patterns may act as markers for the pathological process and indicate the presence of certain diseases. Tears and synovial fluids (hyaluronic acid (HA) solutions) have been investigated by drop deposition and Raman spectroscopy techniques by other groups [10, 11]. Ferning patterns in dried tears were studied by energy dispersive x-ray analysis which showed that inorganic salts make up the branching dendrites and macromolecules were detected on the drop edge due to the evaporation of solvent [12].

Due to the complexity of biofluids, simplified model solutions have been designed and investigated to develop an understanding of the evaporation process of more complicated biological systems. Aqueous solutions of lysozyme have been studied by our group [13], [34] as a biological fluid model system to elucidate pattern formation in drying colloidal sessile droplets. Lysozyme is a globular protein found in high concentration in human tears [14] and saliva [15], which has been studied as a model system for protein crystallization [16], nucleation and solute

self-organization [1]. Simple pure lysozyme solutions displayed ring-like deposits with an undulating interior. The general morphology of the deposits varied little with concentration of lysozyme [13]. Also, large droplets of aqueous lysozyme solution with varying concentrations of sodium chloride have been investigated [37]. The morphology of these deposits was more complicated and exhibited different patterns. Generally the morphology showed a coffee ring structure and cracking on the ring-like structure became obvious with increasing concentration of sodium chloride. Branch-like crystals and a more porous structure were observed in the interior regions.

In this thesis, patterns in the dried deposits of small sessile droplets of lysozyme solutions are studied. Patterns from microdroplet deposits of aqueous lysozyme solution with varying concentrations of sodium chloride are observed and characterized by a digital optical microscope and atomic force microscopy (AFM). Except for the lysozyme/NaCl solution with 0.1wt/100ml NaCl, all the other deposits display an amorphous peripheral ring and complex and varying interior regions. Interesting features and details in certain deposits, such as branch-like dendrites, crystalline forms and porous structures are examined with the atomic force microscope. Scanning electron microscopy (SEM) was used to examine different regions in the drop deposits to help understand the mechanism of evaporation of solvent. Deposits were examined in ambient environmental conditions and in a specific sequence starting on the day they were made. The same deposits of each sample were then intermittently examined over the next two months to monitor pattern stability. The patterns are most stable for low NaCl concentrations (less than 0.10g/100m) and least stable for the very high NaCl concentrations (1.0 g/100ml).

This thesis is organized in chapters as follows. Basic background information on the behavior of drying sessile colloidal droplets is introduced in chapter 1. Chapter 2 discusses the

basic theories of surface tension, the flux equations, and diffusion during droplet evaporation. A literature review is presented in chapter 3, and reviews past studies droplet evaporation, dynamics and phase transitions. Also, pattern formation in biofluid droplets is reviewed as related to the potential application of pattern recognition to disease recognition. The literature on the properties of lysozyme and the effect of salt concentration on colloidal droplets is reviewed. Chapter 4 contains the hypothesis and objectives of the research. Results and discussion from this research are given in chapter 5. Optical and AFM images from micro-scale droplets are documented in a series of fixed aqueous lysozyme solutions with increasing concentration of NaCl. This chapter also describes the details of morphological features and the effects of NaCl concentration on the pattern formation. Assumptions and interpretation related to the growth of certain structures are also provided based on the theories and literature reviewed in chapter 2 and chapter 3.

2.0 THEORY

Several important physical mechanisms related to droplet wetting, evaporation and dendrites growth are discussed in this chapter. In the wetting section, the concepts of surface tension and a diffusion model of droplet evaporation are described. Also, dendritic growth of salt crystals is reviewed in this chapter.

2.1 WETTING

2.1.1 Surface Tension

Surface tension (interfacial energy) has been used to explain the shapes of droplets for two centuries [16]. When the surface of liquid moves outwards, its tension is produced by the cohesion of particles within the liquid. The cohesive forces (such as Van der Waals and electrostatic forces) among liquid molecules lead to an energy imbalance and form an inward net force which decreases surface area [16],[42]. Relative interfacial energies between three phases (gas, liquid and solid) control the equilibrium shape of a droplet which otherwise would be spherical. As liquid evaporates, the interfaces between the three phases deform to minimize the interfacial energies.

γ , is a measure of this energy deficit per unit surface area. At constant temperature and pressure, surface tension can be defined as the change of Gibbs free energy per surface area.

$$\gamma = \left[\frac{\partial G}{\partial A} \right]_{T,V,n} \quad 2.1$$

G is Gibbs free energy, A is the area, V is the total volume, T is the temperature and n is the number of molecules in the system.

2.1.2 Young's Equation

A contact angle exists between the liquid and solid substrate depending on the relative interfacial energies. The interfaces between gas, liquid, and solid phases of a typical drop are illustrated in the schematic in figure 2.1. γ_{LG} , γ_{SG} , and γ_{SL} , are defined as the energy content of the interfaces.

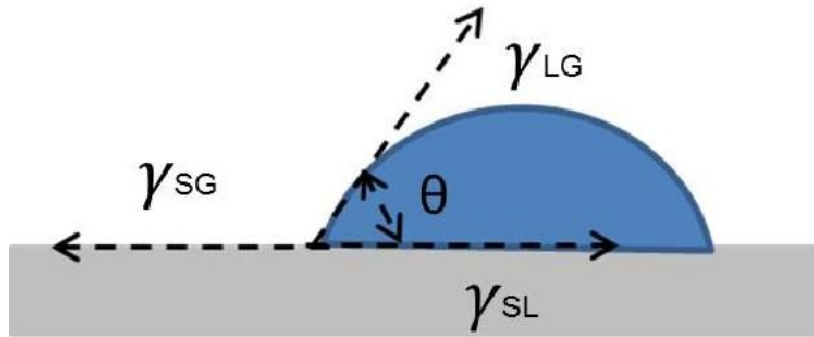


Figure 2.1 .Illustration of interfacial tensions and contact angle of a liquid droplet wetted to a solid surface.

At equilibrium, the sum of the capillary forces on the contact line equals to zero. The equilibrium relationship of interfacial energies and contact angle can be described by Young's equation:

$$\gamma_{SV} - \gamma_{SL} - \gamma_{LV} \cos \theta = 0. \quad 2.2$$

Young's equation assumes that the sessile drop system is in thermodynamic equilibrium on an ideally smooth solid surface and the system is free from contamination [16].

2.2 DROPLET EVAPORATION

2.2.1 Evaporation Model

A widely accepted evaporation model for sessile droplets is the “constant contact diameter” model described by Deegan. In this model, the contact line of a droplet is assumed to be pinned and outward radial fluid flows are induced. With a fixed radius, R , the contact angle and volume of the droplet decreases with time. The schematic in figure 2.2 illustrates the parameters, given a sessile droplet with radius, R , evaporation flux per unit area, J , and contact angle, $\theta(t)$.

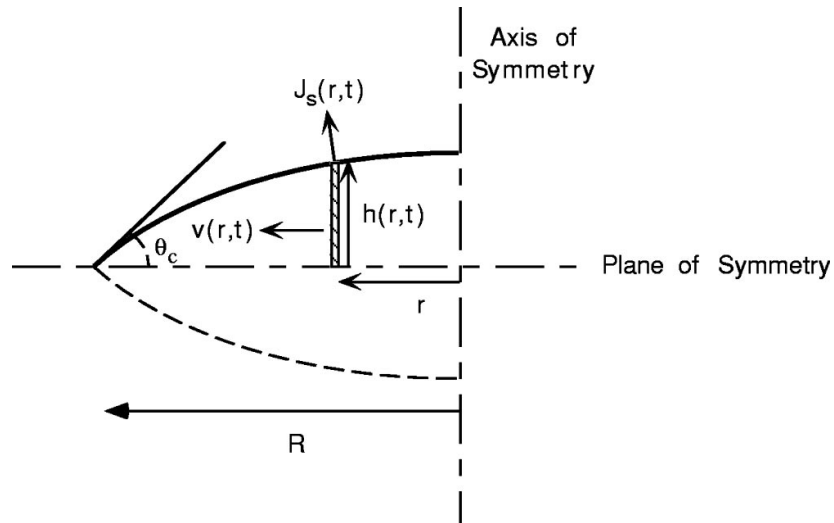


Figure 2.2. Geometry of the model system.

The rate of evaporation of fluid flow is time dependent. In order to determine the rate of evaporation, the droplet height is determined as a function of time and contact angle. Assuming a spherical cap geometry, the height of the droplet, $h(r,t)$ varies as:

$$h(r, t) = \sqrt{\frac{R^2}{\sin^2 \theta(t)} - r^2} - \frac{R}{\tan \theta(t)} \quad 2.3$$

2.2.2 Evaporation Rate

Based on the model evaporation system, the evaporation flux depends on the shape of the drop. In the evaporation process, molecules leave the liquid and enter the vapor phase at the liquid/vapor interface. At the interface, the vapor concentration, c , is assumed to be equal to the saturation concentration, c_s . Since the vapor at infinity is not saturated, the vapor concentration far above the droplet is the ambient concentration, c_∞ . The vapor diffuses outward and the difference in vapor concentration drives evaporation according to the diffusion equation,

$$\frac{\partial c}{\partial t} = D_v \Delta c \quad 2.4$$

where D_v is the vapor diffusivity.

In this diffusion model, the liquid-vapor diffusion process is treated as a steady state problem, where the transient term can be neglected. With these assumptions the diffusion equation reduces to the Laplace equation:

$$\nabla^2 c = 0 \quad 2.5$$

At the liquid/vapor interface, the evaporation flux is expressed by

$$\vec{J}(r, t) = D_V \nabla c. \quad 2.6$$

The evaporation flux is not solved analytically as it is an integral of a nontrivial special function. An analytical solution for the Laplace equation was considered by equating c with the electrostatic potential and J with the electric field. Comparable to Deegan's analytical solution, Hu and Larson derived a finite element method model to describe evaporation. The evaporation rate is expressed as follows:

$$J(r) = \frac{2 D_V (c_0 - c_\infty)}{\pi \sqrt{R^2 - r^2}} \quad 2.7$$

where

$$c_0 - c_\infty = \left(\frac{M_W P_{VS}}{R_g T} \right) (1 - RH) \quad 2.8$$

In the system described in this thesis, M_W is the molar mass of water, P_{VS} is the saturation water vapor pressure, R_g is the ideal gas constant, and T is the temperature.

2.3 DENDRITIC GROWTH OF CRYSTALS

In our research, dendritic salt crystals can be observed in the deposits from solutions containing 0.5g/100ml and 1g/100ml NaCl. A model of dendritic growth of crystals has been proposed by Martyushev *et al* [19]. At the crystal/solution interface, the salt flux density, I at each time τ , is expressed by as a difference in salt concentrations, and given as follows:

$$I = \frac{b(C_s - C_{sat})(C_{s,s} - C_s)}{C_{s,s}} \quad 2.9$$

$C_{s,s}$ is the density of the solid salt and C_s is the instantaneous density of salt in the dendrite cell where crystal growth is taking place. C_{sat} is the saturation concentration of the solution, and b is the kinetic coefficient of crystallization. Based on this salt flux density equation, the impurity flux density in the crystal solution is calculated assuming the impurity is completely expelled by the growing crystal. When C_s reaches C_{sat} , the local system converts to a different phase where no fluxes pass through and crystals cannot continually grow. Also, controlling parameters such as the relative supersaturation, the relative density, and the stability parameter are applied to predict the shapes of dendrites with tertiary branches. The relative impurity content controls the secondary branches of dendrites.

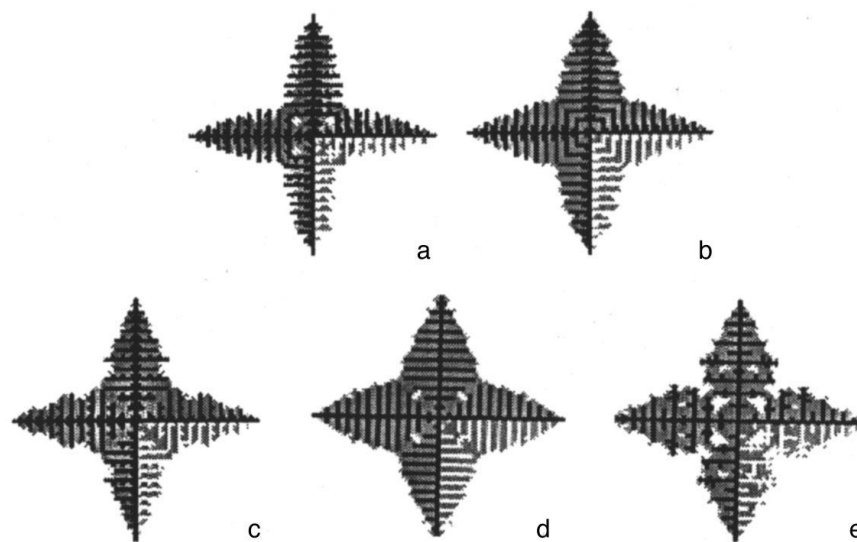


Figure 2.3. Morphology of dendrite growth with increasing relative initial impurity contents from a to e, which show secondary and tertiary branches. The black lines show the salt distribution and the gray region are the impurity transferred to a different phase [19].

3.0 REVIEW OF THE LITERATURE

The phenomenon of droplet evaporation has been studied for many years. As early as 1805, Thomas Young [16] introduced the concept of contact angles between the boundaries of three phases (solid, liquid, and vapor) and proposed an equation ('Young's equation') to explain the equilibrium of the three phases. Much more recently pattern formation from evaporating sessile droplets has become an attractive topic due to its applications in various fields. In this chapter, a review of literature on the pattern formation from colloidal droplets and applications of this technique are elaborated. Also, a review of the properties of lysozyme, the electrolyte mechanism of dried droplets, protein crystallization, and image analysis techniques are provided.

3.1 PATTERN FORMATION IN EVAPORATING DROPS

Suspended particles in colloidal fluids are generally driven to the perimeter of evaporating droplets and accumulate in a peripheral ring due to the "coffee ring effect". Pattern formation in evaporating droplets can be influenced by wetting properties, fluid dynamics, phase transitions, sedimentation, heat transfer, and the physiochemical properties of the solution. The physical mechanisms of evaporating drops and pattern formation have been investigated by a number of research groups. In the following paragraphs, more details are provided.

3.1.1 Evaporative Dynamics and General Pattern Formation

The “coffee ring” form is a general pattern first described quantitatively by Deegan *et al* [1], [17], [18]. They showed that capillary flow induced by evaporation drives the suspended particles in a droplet to the pinned periphery of the droplet where they aggregate to form a ‘rim’. If the contact line is pinned, the contact angle of the drop decreases during the evaporation of solvent. A non-uniform flux (J) is induced as the droplet shrinks (figure 3.1), which increases from the central region to the perimeter as the contact angle decreases. By tracking particles of polystyrene microspheres in water, a relationship between the depth-averaged velocity $v(r)$ and mass of the ring $M(R,t)$ was determined in their research, which can be applied in predicting the morphology of a ring of a drying droplet. Regardless of the chemical properties of solute and substrate, deposition induced by capillary flow could be controlled and predicted. In this picture a prerequisite for the ring formation is pinning of the droplet at the interphase boundary creating a constraint for particles spreading and accumulating.

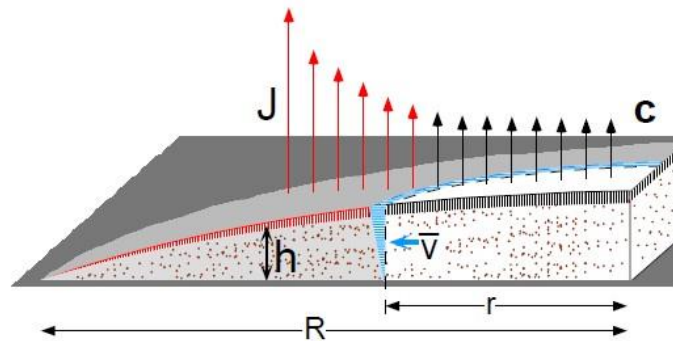


Figure 3.1. Schematic of outward flow of a drying droplet and evaporative flux (J) [19].

Hu and Larson examined the effects of Marangoni stresses on the microflow in evaporating sessile droplets [20]. Induced by the latent heat of evaporation, Marangoni flow is a circulatory flow reversing particles back to the central region, counteracting capillary flow. Suppression of

Marangoni flows is required in the formation of rings. Hu and Larson also described that a pinned sessile drop is a quasi-steady status found to express the evaporation rate [20], [21]. They calculated the evaporative velocity fields by finite element methods with Marangoni-stress boundaries for different contact angles. Surface tension gradients generated by latent heat in the solute affect the deposition patterns on the substrate. They concluded that a positive Marangoni number at a large contact angle can lead to an inward radial flow while a negative Marangoni number at a small contact angle produces to an outward flow.

A variety of experimental systems combining a variety of solvents and solutes have been studied by researchers interested in sessile drop evaporation and particle self-organization. Particles including polystyrene nanospheres and microspheres [22], [23], gold nanoparticles[24], colloidal silica [25] and carbon nanotubes [26–29] in aqueous solutions have been investigated. Also, organic molecules of biofluids have been explored including lysozyme, DNA [8] and serum albumin [2], [29], [31].

Several techniques have been introduced to control the pattern formation. The techniques include evaporative flux [1], [2], contact line depinning [1], [8], particle-substrate interaction [32], [33] and phase diagrams [34]. A numerical model has been proposed by Bhardwaj *et al* [3] combining fluid dynamics, heater transfer and particle transport to simulate the formation of deposits during the evaporation of a nanoliter colloidal solution. Also, researchers have explored various substrates such as glass, mica, silicon wafers, and mercury [22]. When electrostatic interactions dominate, proteins like lysozyme tend to be adsorbed on negatively charged surfaces [36].

3.1.2 Pattern Formation in Micro-scale Droplets

Droplet sizes larger than 1 mm have been well studied in the literature [13], [37], [38]. Shen *et al* [38] examined micron-scale droplets to determine the minimal diameter for coffee ring formation. In drop sizes less than ~ 1 mm, surface tension is dominant and gravitational effects can be neglected. They used aqueous solutions of polystyrene beads particles with three different diameters to produce ring shape deposits with different sizes. Deposits with diameters less than ~ 10 μm did not exhibit coffee ring structures. A minimal size for a ring deposit to form was explained as due to liquid evaporation rates exceeding the diffusion rate of the particles [19].

The impact of gravity is usually considered negligible in much of the literature. Sommer [19] determined that the effects of gravity in a drop with a diameter less than 1 mm and with nano-scale solute particles can be neglected. In our research, the effects of gravity are neglected due to the small size of droplets (diameters less than 50 μm) as well as the nanoparticle suspensions. Although many studies have been done in colloidal drops, little work has emerged in the literature on micro-scale droplets. A full understanding of evaporation dynamics in micro-droplets is not yet established.

3.2 PATTERN FORMATION OF BIOFLUID DROPLETS

Biofluids such as human blood and tear droplets have been studied for years. Due to the complexity of biofluids with components including electrolytes, glucose, or hormones, pattern formations of sessile colloidal droplets of these materials are more complicated to predict and

control. In particular, the components of tears have been investigated [11], [39], [40] in the literature due to its potential application for diagnosis of eye diseases. The evaporation of droplets of human biological fluids leads to deposits with various morphological patterns forming on a substrate. The condensed patterns can act as markers for various diseases reflecting the health situation of a patient. Thus, pattern formation in colloidal drops can be applied to pathogenic diagnosis and medical screening.

Protein concentration in human biofluids such as in blood plasma can reflect some pathological processes which are used in early detection of diseases [41]. Compositional changes usually lead to significant differences in morphology of dried droplets of biological fluids including blood [2], [30], serum, tear [11], [14], [39], [40], etc. As a rapid, simple, and sensitive test for diagnosis, the technique has been applied in various diseases. Detectable diseases include carcinoma, anemia, hyperlipidaemia [2], glaucoma, osteoarthritis [42], etc.

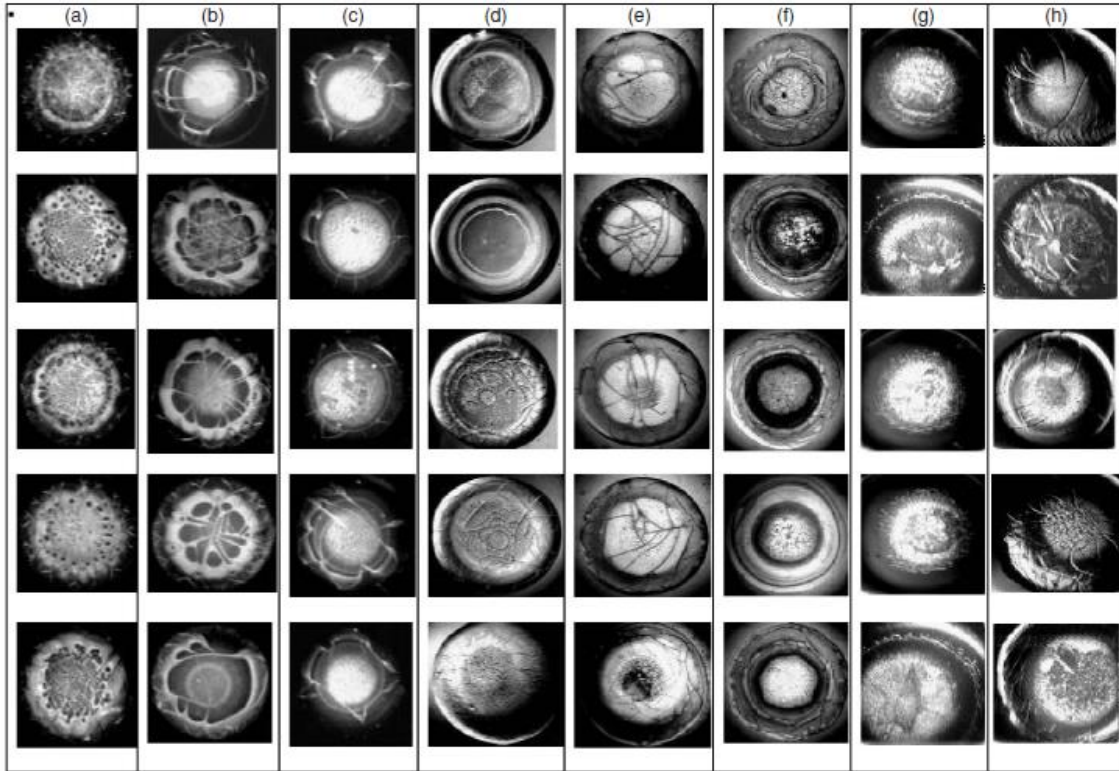


Figure 3.2. The morphological features of dried drops of serum in norm and different diseases: (a) healthy individual (control group); and patients with (b) breast cancer; (c) lung cancer; (d) paraproteinemia; (e) in-time delivery; (f) premature delivery; (g) threatened abortion in different periods; (h) hepatitis [43]

A number of groups [2], [30], [43], [14] have examined the structural properties of the patterns of biofluids droplet deposits and also developed quantitative image analysis methods that attempted to classify patterns of drops. Yakhno *et al* [43] examined and compared the dried deposits of human blood serum with healthy people and those with various disorders. Significant differences in the patterns can be observed between these groups of serum deposits in figure 3.2. They used the dynamics of acoustic-mechanical impedance (AMI) to illustrate that the self-organization process in drying plasma drops can be applied to distinguish normal and pathologic pregnancies as well as in diagnosis of anicteric hepatitis. Similarly, Brutin *et al* [2] studied whole blood droplets of healthy people and patients with anemia and hyperlipidemia respectively

documented in figure 3.3. Large cells in whole blood droplets determined the pattern formation while in serum small proteins and electrolytes control the pattern formation. The morphology of whole blood drop was described by existence of cracks in the corona which are associated with the presence of large solid plaques indicating certain diseases.

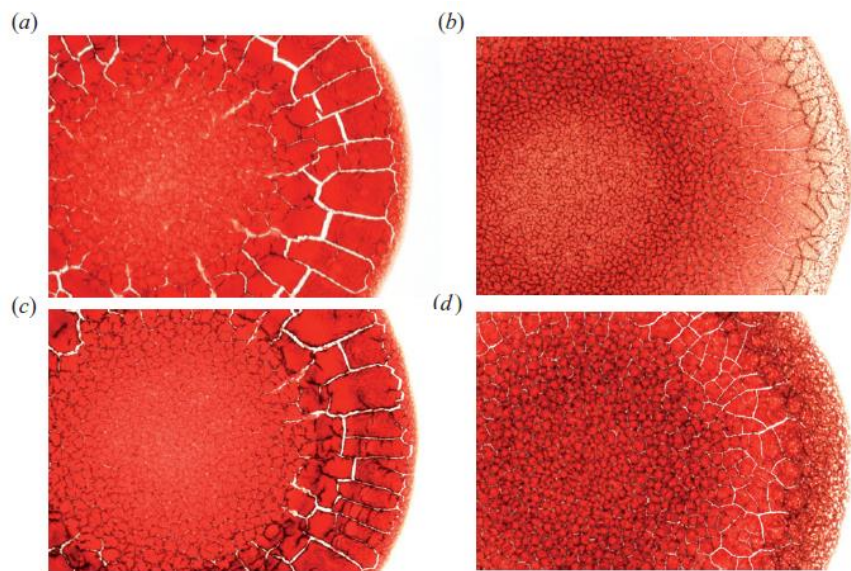


Figure 3.3. (a) and (c) are dried droplets of blood from healthy individuals with different ages, while (b) and (d) are person with anaemia and hyperlipidaemia [2]

In addition, tear droplets also have been studied by groups of researchers [11,12,39,40]. Kuo *et al* [39] classified three different zones of a dried teardrop: central, transitional, and ring zones. The peripheral ring is a zone mainly containing large molecules such as mucins and proteins. Branched fern crystals formed in the central and transitional zones. Based on Raman microspectroscopy, the amount of change of protein in the teardrop was applied to indicate the infectious disease of the ocular surface. Tear fern-like crystals are patterns formed when a tear dries on a clean smooth substrate; they have been shown to be indicative of pathology in many reports. By means of SEM and EDXA, Pearce and Tomlinson [12] found Na, K and Cl within

the tear ferns while sulfur was found at the periphery of the deposit indicating biomacromolecules, proteins and mucin are the main components forming the ring.

Approximately 30 proteins were identified in tears by Sariri and Ghafoori [44]. Changes in proteins and enzyme concentrations in tears can be used to diagnose eye diseases and disorders including enzymopathies, the harmful effects of air pollution, diabetes mellitus and some allergies. The main tear components and their concentrations are presented in Table 3.3.1[44].

Table 3.3.1 Average concentrations of some important proteins and ions in human tears.

Protein	Concentration (mg/ml)	Ion	Concentration (mg/ml)
Lysozyme	2.36	Na ⁺	80-170
Albumin	1.3	K ⁺	6-42
Tear specific pre-albumin	1.23	Ca ²⁺	0.3-2.0
Lactoferrin	1.84	Mg ²⁺	0.3-1.1
Other	0.427	Cl ⁻	106-135
Total protein	7.51	HCO ₃ ⁻	26

Although various spectroscopic methods have been used to detect small changes of proteins in biofluids, they are relatively time-consuming and expensive. The complex compositions of biofluids make identification and diagnostic analysis challenging. However, the deposit of morphology as influenced by the composition of the biofluid may be a simple and inexpensive alternative with great potential on diagnostics. One of the objectives of this research is to

characterize the deposit patterns of droplets of salt/protein solutions in order to facilitate the development of an image recognition software program capable of discerning diseased droplets of biological fluids. This low cost screening method would only require a digital microscope and a computer, ideal for use in underdeveloped regions that do not have access to expensive medical testing laboratories and equipment.

3.3 LYSOZYME

3.3.1 Lysozyme properties

Lysozyme is a small globular enzyme, a type of protein found in many human fluids including saliva, tears, and breast milk. Lysozyme has a molecular mass of 14kDa and crystallizes in a tetragonal form. Due to its high stability and purity, lysozyme is well investigated in terms of protein crystallization [45], [46], [24], [47], [48] and aggregation and protein adsorption [49–52]. With an isoelectric point (pI) of 11.1 [53] and a net charge of +9 per molecule at a pH of 5.6 [50], lysozyme is rather stable and compact with dimensions of 3.0nm x 3.0nm x 4.8nm measured by X-ray diffraction on protein crystals [54]. The main function of lysozyme is to damage bacterial cell walls. Among 30 identified proteins in tears, lysozyme is the most abundant protein (about 31.4% of the total protein and with a concentration of 2.36 mg/mL [44]). Several properties of lysozyme are documented in Table 3.3.2.

Table 3.3.2 Properties of lysozyme

Dimensions	3.0nm x 3.0nm x 4.8nm
Molecular Mass	14kDa
Isoelectric Point	11.1
Diffusion Coefficient	$1 \times 10^{-10} \text{ m}^2/\text{s}$

3.3.2 Electrical properties

Dissolved in water, lysozyme has a wide range of properties depending on solution pH and the ionic strength of added salts. When a pH of around 4.0 to 4.5, lysozyme is positively charged due to its isoelectric point of 11.1[55] and spontaneously adsorbs on to negatively charged substrates such as cleaved mica. Based on the electrostatic and Van der Waals interactions between positively charged lysozyme and negatively charged substrates, the spontaneous adsorption process can be controlled by adjusting the ionic strength to the selected lysozyme concentration. Also, the effective surface charge of lysozyme depends on pH and ion binding [56]. At low pH, chloride binding is highest where lysozyme is most positively charged. When pH increases to the isoelectric point, a less negative binding occurs where the protein net charge depends less on ionic strength. Preferentially, lysozyme interacts with up to 12 chloride ions at pH 2.5[56].

3.3.3 Transport Properties

The diffusion coefficient of lysozyme is a function of the concentration of the lysozyme solution [57]. At low volume fractions of 0.01, the diffusion coefficient of lysozyme is of the order of 10^{-10}

10^{-10} m²/s. When the volume fraction increases to 0.1, the diffusion coefficient decreases to 5×10^{-11} m²/s. Above this volume fraction, the interactions between lysozyme molecules become dominant. Also, the pH of the solution greatly affects the diffusion coefficients [57]. For pH 7.4 - 7.8, lysozyme molecules form aggregates which do not form at a pH of 2.9 - 3.0.

3.3.4 Aggregation and crystallization

Due to the stable solid phase of lysozyme and interesting gel and liquid phases of lysozyme solutions, many studies have focused on aggregation[37],[58], [59] and crystallization[46], [47], [58]. The driving force for crystallization of lysozyme is the degree of supersaturation. When the protein concentration is greater than the equilibrium concentration, the crystalline phase occurs. Lysozyme crystals are usually grown from aqueous sodium chloride solutions resulting in a tetragonal structure, “sea urchin” structure or orthorhombic structure depending on temperature and supersaturation [46], [61], [62], [63]. Recently, Liu’s research has examined the nucleation kinetics of lysozyme crystal growth. Different crystal shapes were described depending on various solution conditions: concentrations of protein and NaCl and temperature. The different crystal shapes of lysozyme corresponded to different growth rates of (110) and (101) crystal facets [63]. As the concentration of salt rises, the protein-protein interactions are more attractive. Other research has examined the liquid-liquid phase separation and sol-gel transition of supersaturated lysozyme solutions, which are intrinsic features for globular proteins [64]. They also determined that the L-L phase separation enhances the lysozyme crystal nucleation rate. A postulated phase diagram for globular proteins is provided to illustrate the phase transitions depending on temperature and protein concentration.

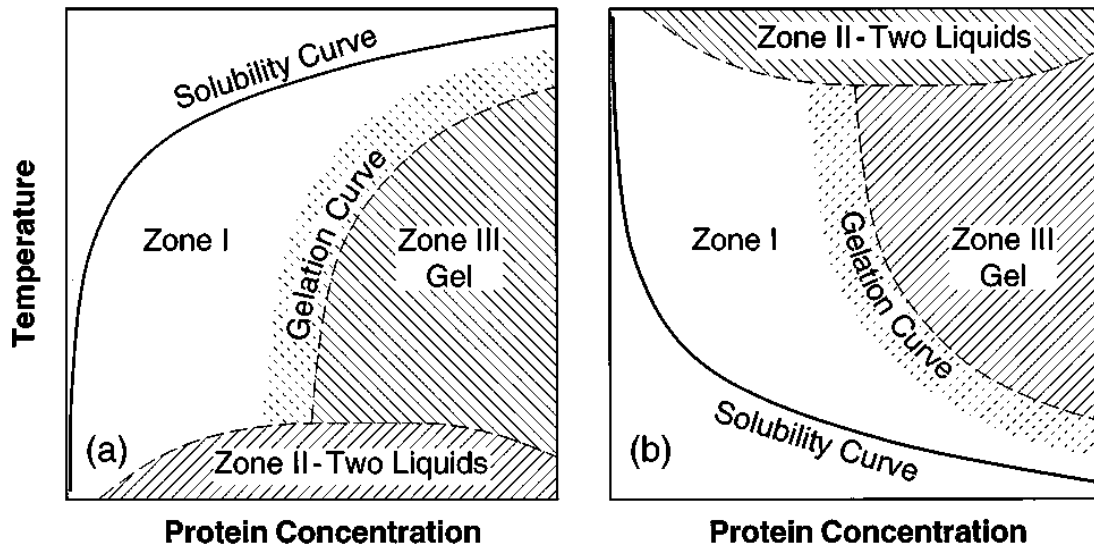


Figure 3.4. Postulated phase diagram for globular proteins. (a) normal solubility (b) retrograde solubility. Zone I is region for protein crystallization. Zone II: liquid-liquid phase separation. Zone III is a region of gelation [64].

Cardinaux's study [65] showed that dynamical arrest is the main reason leading to the gel and glass phases of lysozyme. These transformations happen under the requirement of a separation of protein-rich and protein-poor phases before the dynamic arrest can occur. Gelation may happen in a dilute solution dense percolated glass phase. It has been verified that the jamming and kinetic arrest of colloids correspond to gelation and the glass transition [66]. More detail on phase transitions is provided in the paragraph 3.4.

Phase separation in lysozyme solutions is related to protein-protein interactions of lysozyme molecules with short range attraction and long range repulsion in competition. The short range attraction includes van der Waals, hydration interactions while the long range repulsions are electrostatic interactions and the net charge of the protein and ionic strength of solution [65]. In high supersaturation solutions, plate-like crystals of lysozyme grow while the tetragonal lysozyme crystal is elongated in the low supersaturation solution [63]. Besides

supersaturation affecting the crystal shape of lysozyme, the pH plays a role. Single tetragonal crystals are formed at low pH, and “needle-like” crystal grows when the pH increases [64].

3.4 PHASE TRANSITIONS IN EVAPORATING DROPLETS

When solvent in a colloidal droplet evaporates, the solute concentration increases which changing the physical and chemical properties of the droplet and affects the pattern formation of the droplet. Suspended particles in a solvent aggregate until a network is formed and a sol-gel transition occurs. Gelation has been explained by several scenarios including DLCA (diffusion limited cluster aggregation), kinetic or dynamic arrest, phase separation, percolation and jamming [69]. Lu *et al*'s research considered that for isotropic short-range interactions which are van der Waals forces, surface chemistry, hydrophobic effects and some depletion interactions, gelation is triggered by spinodal decomposition which is a phase separation process driven by a thermodynamic instability. Gel transitions have been studied in sessile drops of solutions including polymer solutions [4], [67] and biofluids [31],[37],[43]. In these studies, radial crack patterns in the final deposits were observed indicating that a phase transition had occurred. Generally, the gel transition begins at the droplet edge and gradually moves inward to the center as the solvent evaporates in the central region. A gel-like skin is formed in all the area of a droplet deposit as the remaining liquid evaporates. The glassy skin was described in droplets of whole blood [30] and ellipsoidal particle suspensions [68].

3.5 EFFECT OF SALT CONCENTRATION ON PROTEIN PATTERN FORMATION

Electrolytes play an important role in protein pattern formation. Researchers have observed crack patterns of colloidal droplet induced by electrolytes [31]. Depending on the salt content in the solution, the crack patterns varied. More complex salt-induced protein patterns were studied [67]. Salt-induced protein patterns including rosette, scalloped, Chinese arrow-like and dendritic shapes were observed in bovine serum albumin salt solutions. At low salt concentration, dendritic aggregates are dominant while at high salt concentration, rosette-shaped protein patterns formed. Two modes have been found relating the evaporation rate to the morphology of protein patterns: edge-enhanced evaporation for low salt concentration solutions and center-enhanced evaporation for high salt concentration solutions [67]. Kaya *et al* [68] examined salt crystallization in evaporating droplets of polyelectrolyte and salt solution. Complex crystal structures including fractals, dendrites, periodic concentric rings, needlelike crystals, and small triangular-shaped crystals were observed. The morphologies for these biofluid deposits containing salts are similar: a peripheral ring and a central region with crystallites. A general view [12] concludes that the components of salt-protein solutions separate during the evaporation of the droplet and the protein tends accumulate at the periphery while the salts segregate to the majority in the central region.

4.0 RESEARCH DESCRIPTION

4.1 HYPOTHESIS

The primary hypothesis of this thesis is that by changing the NaCl concentration in the lysozyme-based deposits will result in reproducible and interpretable variations in the self-assembled patterns formed from evaporation of micro-sized biofluid droplets. A supplementary hypothesis is that evaporative patterns from simplified biofluids can act as a “fingerprint” for identification based on solution chemistry. This work will provide guidance on interpreting the patterns from micro-size ($<50\mu\text{m}$) colloidal fluid evaporation and support of the idea that the detailed morphology of the patterns may function as biomarkers of various physical interactions [37].

4.2 OBJECTIVES

The primary purpose of this thesis is to describe and explain the pattern formation of micro-scale droplets of solutions at fixed lysozyme concentration for different NaCl concentrations by using atomic force microscopy. Structures with complex morphologies including peripheral rings, dendrites, pores and cavity patterns are found in certain ranges of salt concentration. These

features may serve as fingerprints of biofluid chemistry and thus potentially enable disease detection and recognition. By modeling a simple drying droplet system, the evaporative behavior of sessile colloidal drops is studied and explained using fluid dynamics, phase transitions, particle transport and self-organization. Also, by monitoring the same samples over two months after they have been made, the stabilities of the samples are examined.

The objectives of this thesis can be summarized:

1. To document and interpret the morphological features of micro-scale drying droplets from different concentrations of lysozyme and NaCl.
2. To document the role of solution chemistry on pattern formation.
3. To assess the stability and time dependence of the patterns formed.

5.0 EXPERIMENTAL DETAILS

5.1 SOLUTION PREPARATION

Aqueous protein solutions were prepared by dissolving high-purity lysozyme powder (Sigma Aldrich, L6876) in deionized water (18.2M Ω .cm) at 35 °C to a concentration of 2.0g/100mL. A series of aqueous sodium chloride (NaCl) solutions were also prepared in concentrations ranging from 0.02g/100ml to 2g/100ml. Using deionized water and the stock lysozyme and salt solutions, a series of binary solutions containing 1.00 wt% lysozyme (ϕ_L) with sodium chloride concentrations (ϕ_N) ranging from 0.01 to 1.00 wt% were prepared.

Table 5.1. Summary of solutions studied

Solution Name	ϕ_N (g/100ml) (with a fixed ϕ_L (1g/100ml))
L100	0
LN001	0.01
LN005	0.05
LN010	0.10
LN025	0.25
LN050	0.50
LN100	1.0

All solutions were stored at 2 °C and brought to room temperature before droplet deposition. Commercial lysozyme powder is purified from chicken egg white. The protein content by UV absorbance is 90% buffered with ~10% salts such as sodium acetate and sodium chloride. Also, 46 moles of chloride per 1mole of lysozyme is measured by using X-ray fluorescence according to the product description.

5.2 SUBSTRATES AND DEPOSITION TECHNIQUES

With a high reflectivity and a relatively smooth surface, silicon wafers were chosen as the standard substrate for droplet depositions in this work. Lysozyme-NaCl deposits are nearly transparent which makes glass substrates problematic for both AFM and reflection optical microscopy. The silicon wafer solves this problem due to its good reflective properties making the droplet visible on the substrate. Note also that the silicon wafer surface is expected to be negatively charged [49] which attracts the positively charged lysozyme molecules enhancing the droplet pinning. Researchers have studied adsorption of lysozyme on silica [72], [73], and found out that lysozyme adsorbed on the silica substrate in monolayers.

Silicon wafers were ultrasonically cleaned (first isopropyl alcohol (IPA), followed by acetone, and then DI water, and finally blown dry with compressed air). Microdroplets of solutions were sprayed on cleaned silicon wafers using a nebulizer (Preval®). The droplets evaporated under ambient conditions in a climate-controlled laboratory with a temperature of 25 °C and relative humidity of around 30%. The Preval® aerosol spray system produced the droplets with diameters from ~ 10 µm to 250 µm.

5.3 OPTICAL MICROSCOPY

In this experiment, we use a digital optical microscope (Keyence, VHX-600) in bright field reflection mode to observe and measure the droplets. The color was adjusted by setting the white balance and “image enhancement” mode was selected to collect images with enhanced contrast. For detailed analysis and comparison individual droplet images were recorded at a magnification of 3000X. Typical examples of lower magnification images of the overall droplet patterns produced by the aerosol spray system are shown in Figure 5.1.

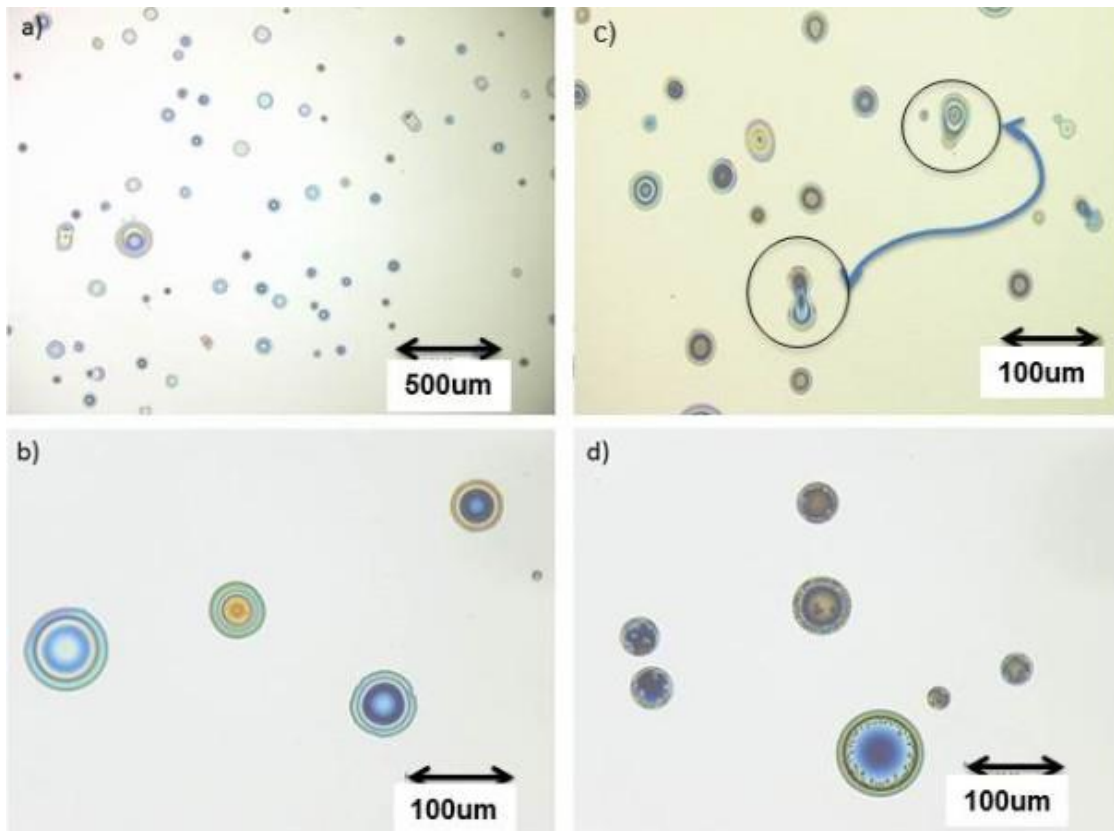


Figure 5.1. Reflection optical microscopy images illustrating typical droplet sizes produced by aerosol deposition of lysozyme solutions a), b) $\rho = 1.0 \text{ g}/100\text{mL}$, c) $1.0\text{g}/100\text{mL}$ containing $0.5\text{g}/100\text{mL}$ NaCl, d) $1.0\text{g}/100\text{mL}$ containing $0.25\text{g}/100\text{mL}$ NaCl. a) $\times 100$; b)c),d) $\times 500$.

In addition to the requirement that the drops studied should be small enough for scanning in our AFM (less than ~ 50 micron diameter) other limitations were also imposed. First, drops that did not have circular or very nearly circular perimeters were excluded. In Fig. 5.1 one can observe interesting distortions in closely neighboring drops and overlapping of these drops are observed in the low magnification images, which can be found in Fig.5.1(c) (marked with black circles). The evaporation rate is lowest at the overlap of the vapor field of two neighboring drops which causes disruption in the evaporative flux and leads to a depinned larger drop. There was also a tendency to select ‘representative’ drops illustrating the main features of the majority of the drops for a particular concentration.

5.4 ATOMIC FORCE MICROSCOPY

Atomic force microscopy (AFM, Digital Instruments, D3100) was used to characterize the detailed morphology of micro-sized droplets. AFM is a form of scanning probe microscopy (SPM) which is used here to measure the topography of entire drops, local roughness and cross-sectional profiles of the deposits.

Tapping mode AFM was used in this experiment. Compared with the Non-contact AFM, tip in contact mode contact is oscillated near its resonant frequency through the adsorbed fluid layer on the surface and the cantilever. In the Non-contact mode, the tip does not contact the sample surface, but oscillates about the surface which leads a decrease of resonant frequency of the cantilever.

In tapping mode the AFM operates by scanning a tip attached to an oscillating cantilever across the sample surface. A standard tip is used which lightly taps on the sample surface during scanning while the cantilever is oscillated at its resonance frequency with an amplitude round 20 nm to 100 nm. The feedback loop electronics are found in Figure 5.2 which illustrates the detection and maintenance of the oscillation signal acquired by the split photodiode detector. The scanner is a piezoelectric which manipulates the probe in x, y and z directions. The vertical position of the scanner at each (x, y) data point in order to maintain a constant “setpoint” amplitude is stored by the computer to form the topographic image of the sample surface. By maintaining the oscillation amplitude, a constant tip-sample interaction is maintained during imaging.

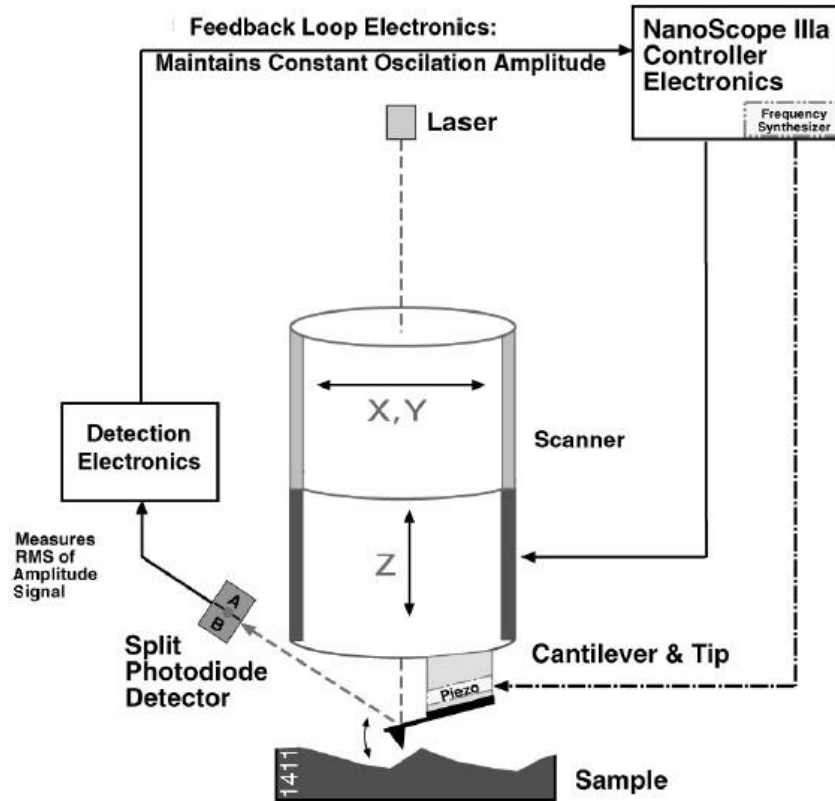


Figure 5.2. Basic setup schematic for SPM system.

Selected droplets with diameters less than 50 μm were characterized in air by AFM with a standard tip (K-TEK Nanotechnology, LLC, NSG01). At least 10 drops from each solution concentration were imaged by optical microscopy and AFM in ambient conditions. AFM data was analyzed with Gwyddion SPM software to extract the critical dimensions, RMS roughness, and cross-sectional profiles. Several methods were applied to modify and improve the AFM images. First, scanning defects such as artifacts and scan lines were removed. Then, for small abnormal pixels caused by error data, a hyperbolic flatten function was used to interpolate the pixel information from the surrounding area. The corrections for the pixels do not suppress the features or texture of the surface. Finally, the minimum pixel value was set as the plane of the substrate.

5.5 EXPERIMENTAL UNCERTAINTIES

The uncertainties in this experiment are of two types. First is the possible variation of lysozyme droplet concentration. Even though all the lysozyme droplets were prepared and deposited using the same procedures, the micro-sized droplet concentrations might be slightly different due to evaporation during the time required to reach the substrates. Second, AFM measurement uncertainties should be mentioned. The local uncertainty can be estimated from instrument calibration data. By analyzing through Gwyddion, the measurement uncertainty is added to results through the statistical function as the data is processed.

6.0 RESULTS AND DISCUSSION

In this Chapter, optical microscopy images and AFM analysis of various lysozyme-based deposits are presented for series of NaCl concentrations from low to high. The result images include 2-D and 3-D AFM topographic maps, cross-sectional height profiles and detailed images of the central and ring regions. Morphology descriptions are focused on two regions: the central region and the outer ring. Also, a basic interpretation of pattern formation is given in this chapter.

6.1 RESULTS FROM L100 TO LN100

6.1.1 L100

The generally observed morphology of the dried drop residues from lysozyme aqueous solutions with a concentration of 1wt/100mL is documented in Figure 6.1.

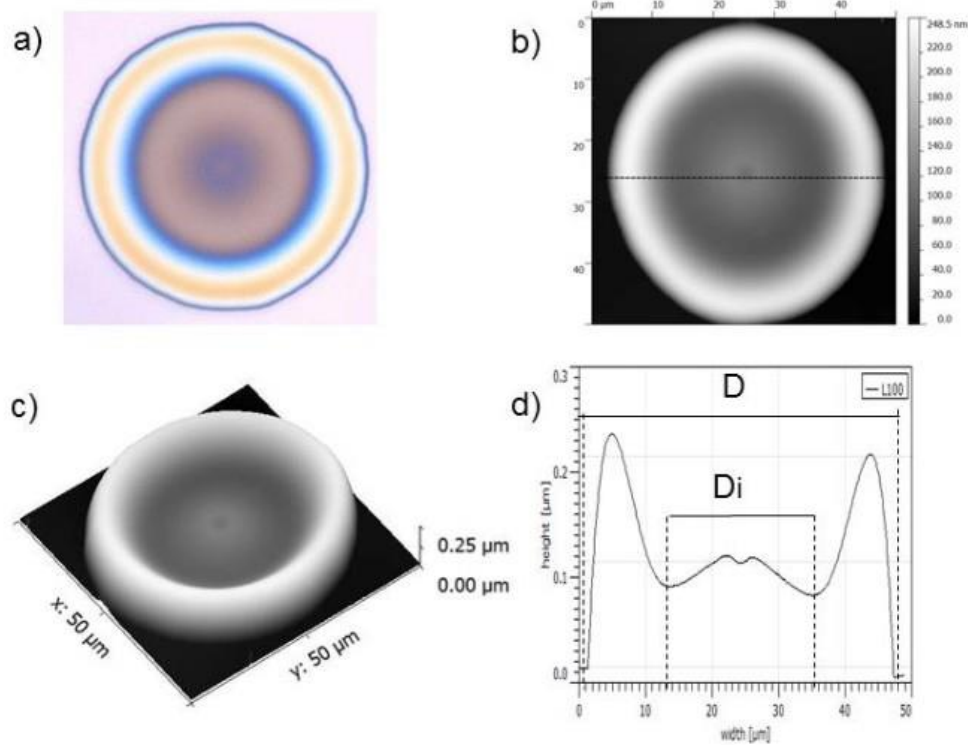


Figure 6.1. Representative image of a lysozyme drop deposit with $\rho = 1.0 \text{ g/100 mL}$. (a) Optical microscopy image; (b) 2-D AFM topographic map with $50\mu\text{m} \times 50\mu\text{m}$ area; (c) 3-D view of AFM topography data; (d) Cross-sectional height profile.

For ease of discussion, regions in the deposits are distinguished and referred to as “Region I” and “Region II”. Region I is a peripheral ring and Region II is the central region with a mound-shape and a small dip in the center. The deposit is radially symmetric with a peripheral ring which is much thicker than the drop interior as illustrated in the cross-sectional height profile (figure 6.1d). The height of the ring suggests that during the evaporation of solvent the majority of solute aggregated at the pinned periphery due to the capillary flow.

From Region I to Region II, the thickness decreases sharply to a minimum and then rises gradually to form a mound with a small depression at the center. Two diameters were measured, the outer drop diameter D , and the inner diameter between the two minima, D_i . The width of the

ring, w is defined as $(D-D_i)/2$. Finally, the relative size of the ring, w/D is calculated to quantify the morphology of droplet deposits. The average w/D for pure lysozyme deposits is 0.26 from analyzing data from 5 deposits. According to previous research in our lab [13], the relative size of the ring is independent of concentration for lysozyme aqueous solutions. Also, the maximum height of the ring (h_r) and an average height (h_c) of the central region are measured. The ratio of the heights of a droplet deposit, h_r/h_c is 2.3, on average, for 1wt% lysozyme aqueous solution droplets.

6.1.2 LN001

The dried droplet deposit for 1 wt% lysozyme solution containing 0.01 wt% sodium chloride solution is documented in figure 6.2.

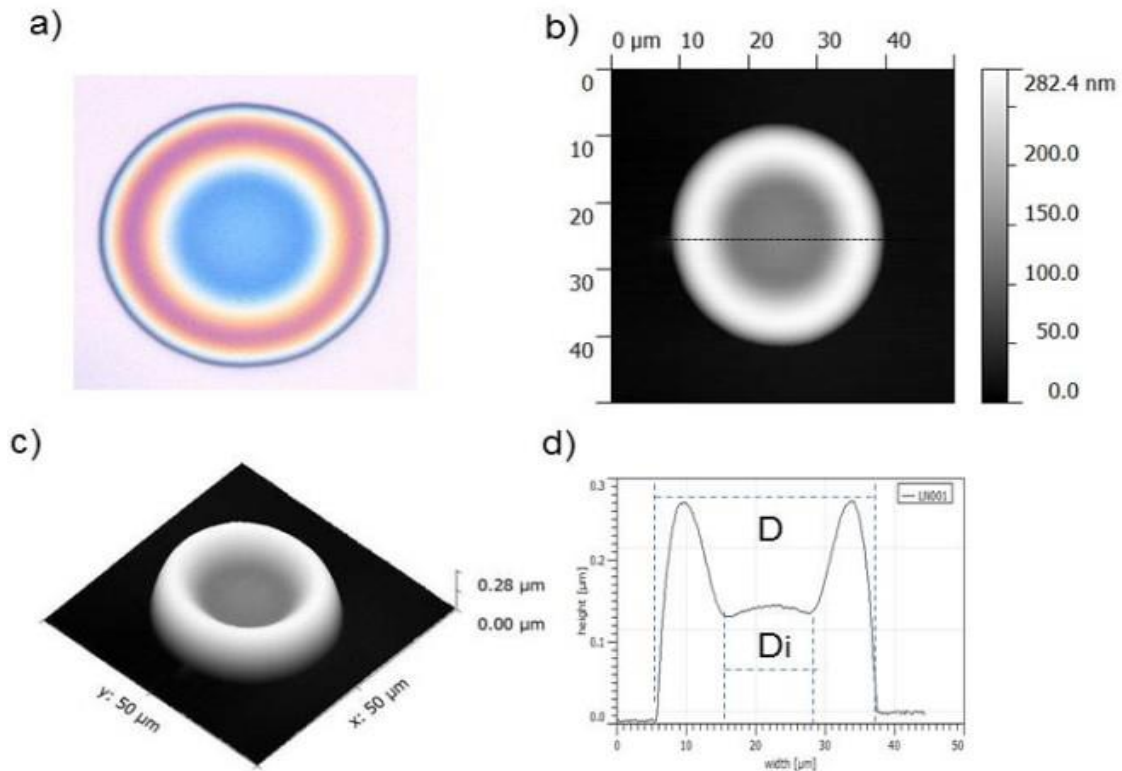


Figure 6.2. Representative image of a lysozyme-based drop deposit containing 0.01 wt% NaCl. a) Optical microscopy image; b) 2-D AFM topographic map with 50µm X 50µm area; c) 3-D view of AFM topography data; d) Cross-sectional height profile.

Similar to the lysozyme deposit with concentration of 1g/100ml, the deposit containing 0.01wt% NaCl shows a cap-like or mound structure in the central region and a peripheral ring. The whole deposit is again radially symmetric. An obvious difference between pure lysozyme droplet deposit and the deposit containing 0.01wt% NaCl is the absence of a small depression or pit in the very center of region II (see figure 6.2d). Compared with the pure lysozyme deposit, the deposit containing 0.01wt% NaCl has a relatively wider ring. The average value of w/D is 0.34 from analyzing data from 5 deposits, which verifies that the ring of the deposit containing 0.01wt% is significantly wider. Also, the surface of the deposit is rougher than the pure lysozyme deposit. There is no porous structure or small NaCl crystals found in both regions. The average value of

hr/hc is 1.61. The addition of a very small amount of salt to the basic lysozyme solution appears to limit the growth of the peripheral ring and keep more of the deposit in the central region.

6.1.3 LN005

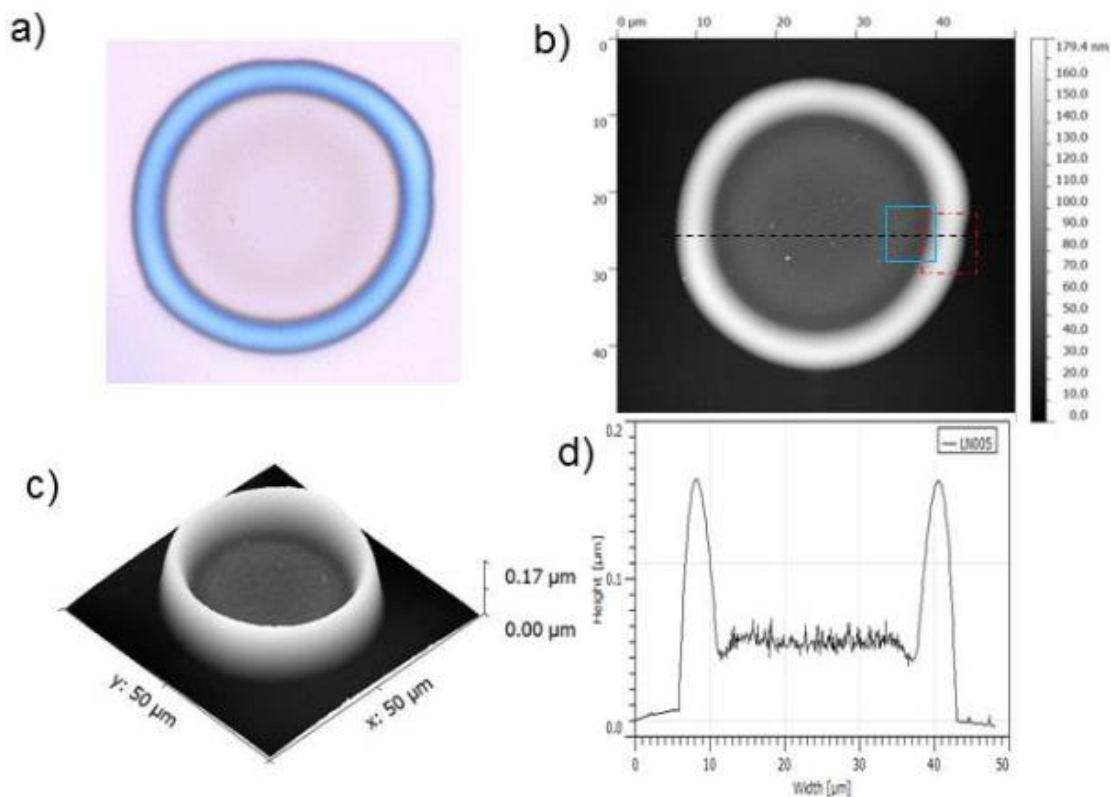


Figure 6.3. Representative image of a lysozyme-based drop deposit containing 0.05 wt% NaCl. a) Optical microscopy image; b) 2-D AFM topographic map with 50µm X 50µm area; c) 3-D view of AFM topography data; (d) Cross-sectional height profile.

Figures 6.3 (a) and (b) are representative images (optical and AFM) of the lysozyme-based droplet deposit containing 0.05% NaCl. Small and shallow pore-like structures are observed on the peripheral ring, which cover the ring and fade away gradually as the height of the ring decreases and disappear at the lowest region. A minimum height is found at the junction between

Regions I and Region II, which appears as a dark ring just to the inside of the peripheral rim (see figure 6.3b). Also, a very slight depression is displayed in Region II. Compared with the deposits described above, the central region is much rougher than at lower concentrations of NaCl though neither pore-like structures nor large crystals are observed. Figure 6.4 (e) and (f) show in greater detail the center region and the peripheral ring. The value of w/D is 0.16 indicating that the ring of these deposits is now relatively narrow. The average height ratio is 2.97, which reveals that the ring of deposit of lysozyme solution containing 0.05% NaCl is quite sharp.

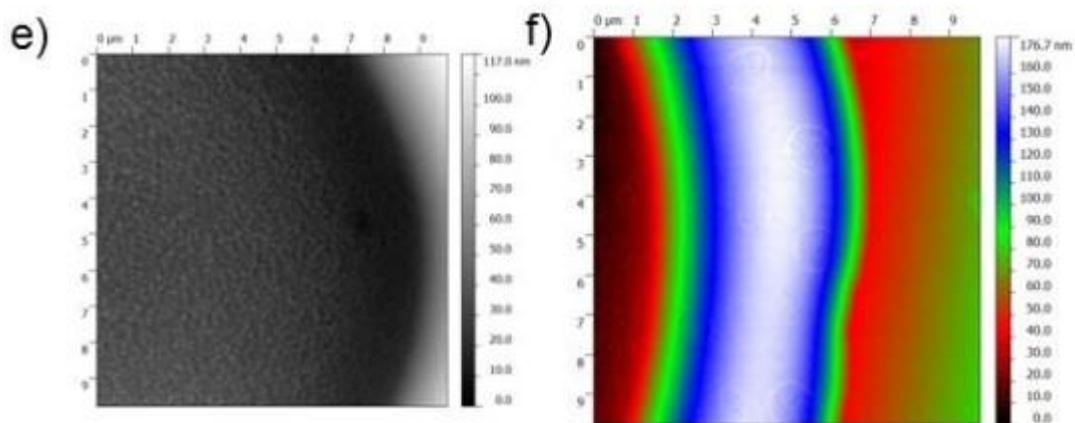


Figure 6.4. e) Detail view of deposit interior, AFM topographic map (10 μm X 10 μm); f) detailed view of peripheral ring, AFM topographic map (10 μm X 10 μm).

6.1.4 LN010

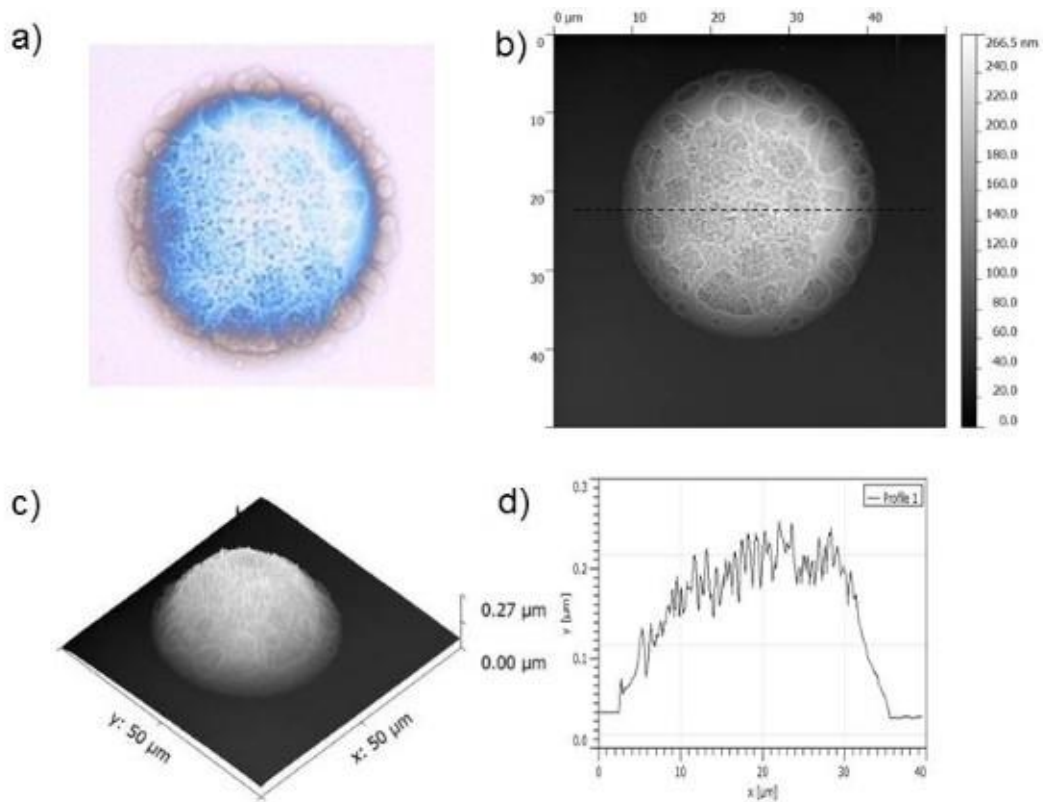


Figure 6.5. Representative images of pattern 1 of the deposit from the standard lysozyme solution with a NaCl solution concentration of 0.10 wt%. a) Optical microscopy image; b) 2-D AFM topographic maps (50 μm X 50 μm); c) 3-D view of AFM topography data; d) Cross-sectional height profiles.

Figure 6.5 shows the pattern one of deposit of lysozyme-based solution containing 0.1wt% NaCl. Starting at this concentration of NaCl, rounded but irregularly shaped pore structures are observed around the periphery of the drop residue. In the interior of the pores one can observe an irregular granular or perhaps particulate aggregate. The pore-like structures noted in 0.05 wt% NaCl are now much larger and more obvious. The inner part of the deposit appears to consist of merged pores so that this region is mainly made up of the granular aggregate mentioned above.

From the AFM images and profile, it is clear that at this concentration of NaCl the distinct peripheral ring is no longer present for micro-scale droplets. Figure 6.5(d) is profile taken through the center of both deposits. The increase in surface roughness associated with higher NaCl concentrations is quite clear. By comparing the morphology of many drops it was determined that smaller drops ($< 30 \mu\text{m}$) generally exhibited a simple mound shape while larger drops begin to exhibit a small depression in the central region which is pattern 2 for the deposits (see figure 6.6). Due to the rapid evaporation speed, microdroplets dry in microseconds and there is little time for the particles in the drop to spread and aggregate on the edge. The same deposits have been checked again on the AFM as well as on the digital optical microscope after one month and display little difference from the measurement made immediately after deposition. In this sample, values of w/D and h_r/h_c are not provided due to the absence of peripheral ring.

For a deposit in this solution with a bigger diameter ($> 50\mu\text{m}$), a peripheral ring is observed in our experiments and is illustrated in figure 6.7. Larger deposits maintain the peripheral rings and porous structures on the edge of deposit. A hypothesis for the disappearance of peripheral ring for micro-scale deposit is that sodium chloride crystallizes within the lysozyme aqueous solution and damages the gel phase or the gel “skin” formed by colloidal solvents. As described in section 3.1, during the evaporation of colloidal droplets most of the electrolytes tend to stay in the central region while macromolecules deposit on the edge. Thus, more ions in the central region coexisting with less protein lead to a region which is rougher than the peripheral region which contain more protein and less NaCl.

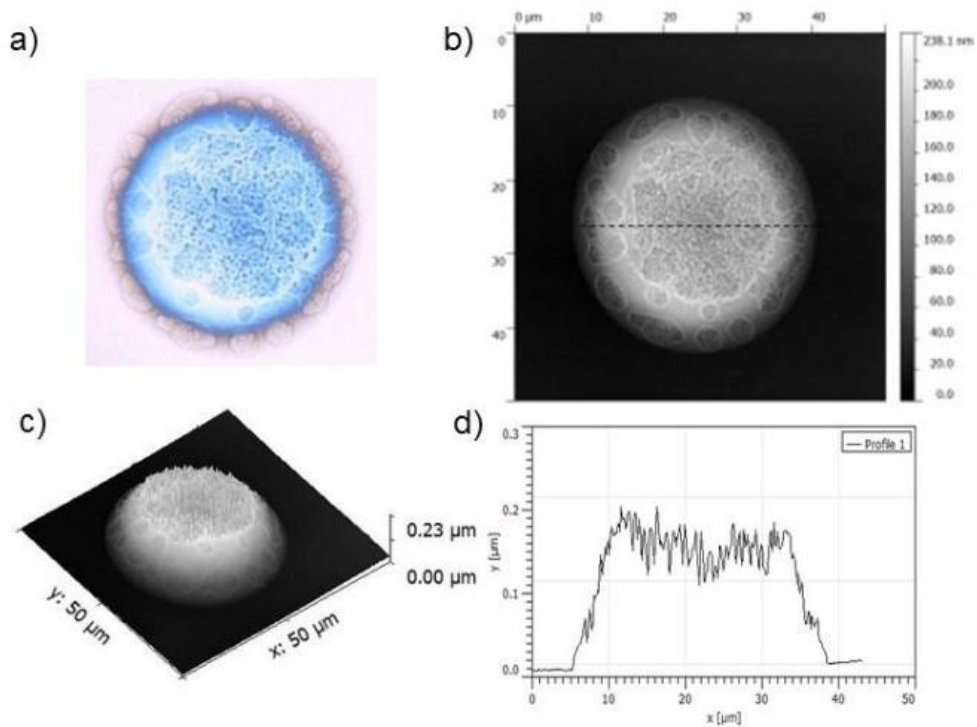


Figure 6.6. Representative images of pattern 2 of the deposit from the standard lysozyme solution with a NaCl solution concentration of 0.10 wt% with a diameter $> 30 \mu\text{m}$. a) Optical microscopy image; b) 2-D AFM topographic maps ($50 \mu\text{m} \times 50 \mu\text{m}$); c) 3-D view of AFM topography data; d) Cross-sectional height profiles.

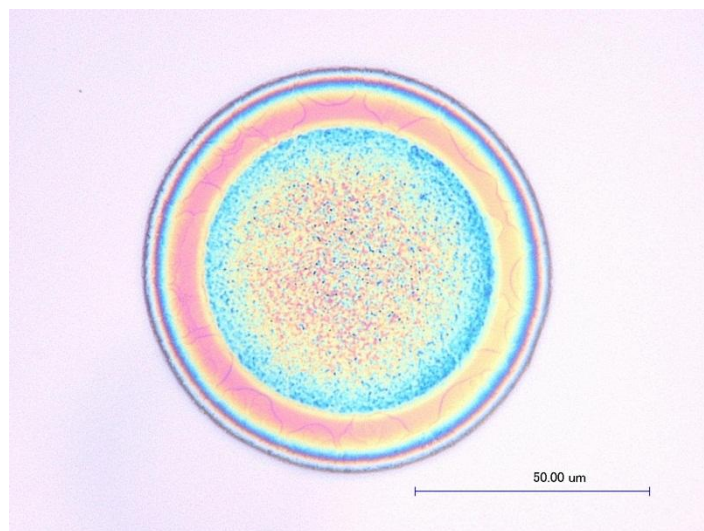


Figure 6.7. Optical image of a larger diameter ($\sim 50 \mu\text{m}$) lysozyme deposit containing 0.1% NaCl.

6.1.5 LN025

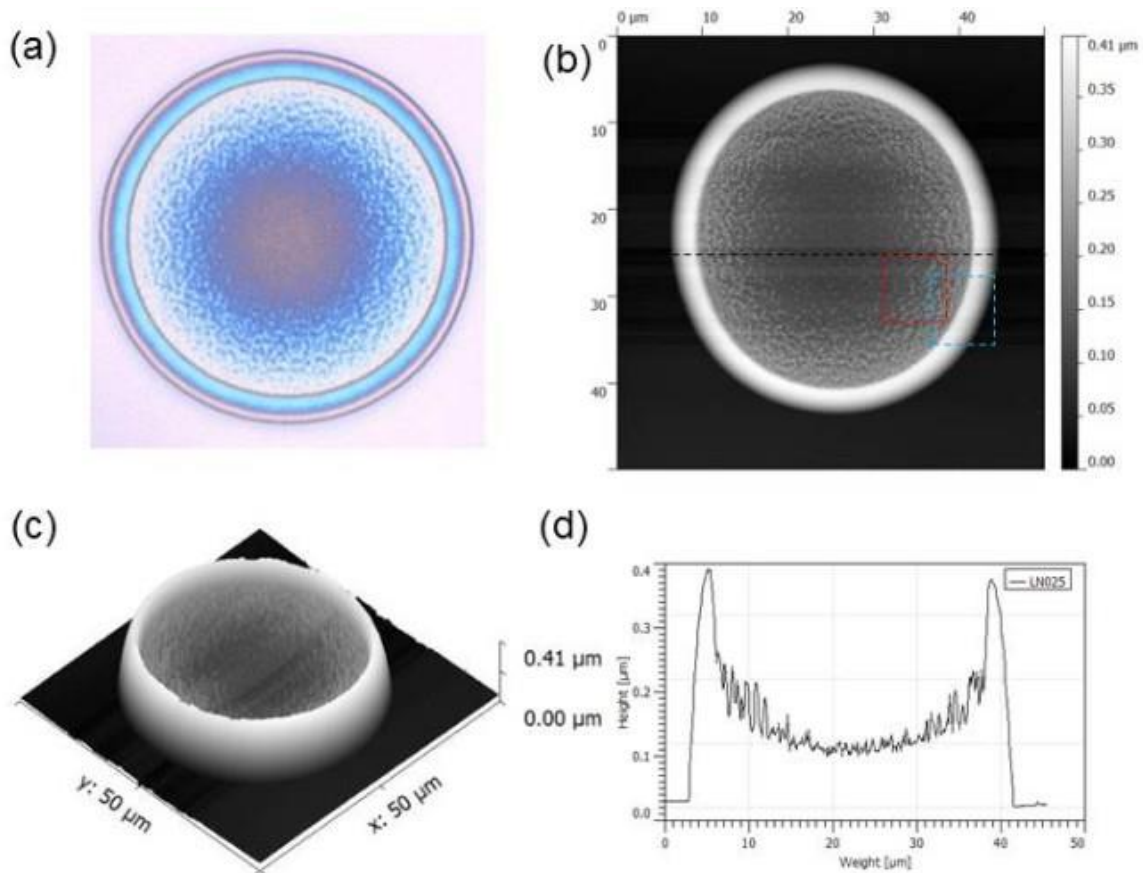


Figure 6.8. Representative image of a lysozyme-based drop deposit containing 0.25 wt% NaCl. a) Optical microscopy image; b) 2-D AFM topographic map with 50µm X 50µm area; c) 3-D view of AFM topography data; d) Cross-sectional height profile.

Figure 6.8 a), b), c), d) and figure 6.9 e), f) show a lysozyme-based deposit containing 0.25wt% NaCl immediately after deposition. The optical image and AFM data were all obtained on the day when the sample was made. Similar to other deposits, the deposit is radially symmetric with a peripheral ring. Instead of a mound in Region II, a depression is observed and illustrated in the cross section height profile. The height of the deposit decreases gradually from the edge to the very center and the minimum height is formed in the very center even though the slope of region

II is not sharp and no large crystals are found. Besides, the small crystals found in region II, aggregated granular structures can be observed in Fig. 6.9e (marked with a red dash square in Fig. 6.8b), which can be considered as a sign of the evolving status of the pore-like structure. Figure 6.9f shows that more aggregation near the edge than that in Region II (the red region versus the green region in Fig. 6.9f). Also, semi-circular shallow pore-like structures can be found on the ring surface. The average w/D is 0.11 and the average h_r/h_c is 2.69.

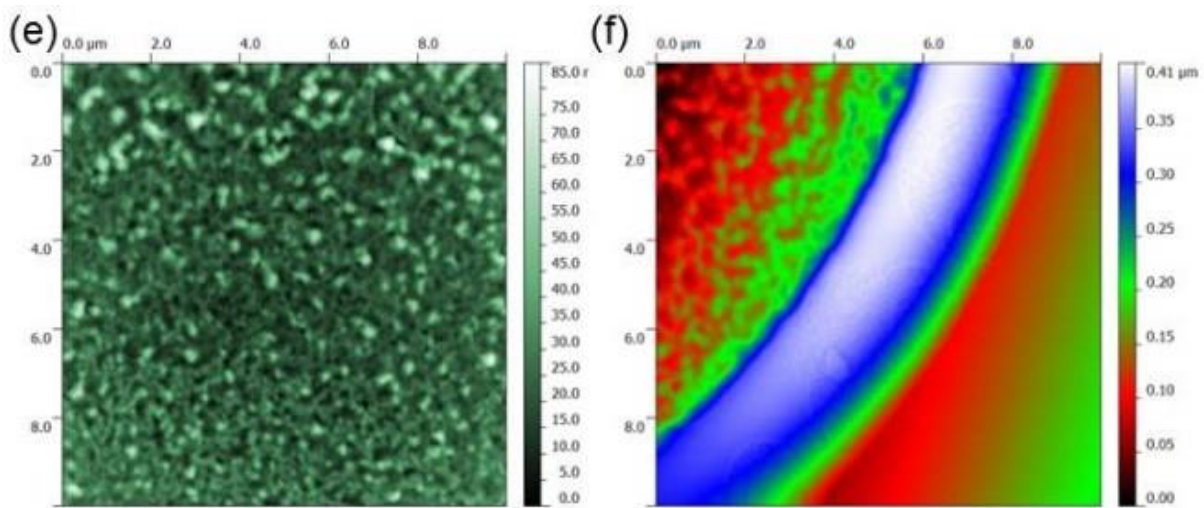


Figure 6.9. e) Detail view of deposit interior, AFM topographic map (10μm X 10μm); f) Detailed view of peripheral ring, AFM topographic map (10μm X 10μm).

Figure 6.10 (a – d) shows clear evidence that at this concentration we begin to see substantial changes in the droplet patterns after one week stored under ambient conditions. Ramified structures that appear to be aggregates of small particles are now observed in the central region and crossing onto the peripheral ring. These aggregates are stable once formed and do not change significantly over the next month. The cross section height profile (Fig. 6.10d) shows that the maximum height of the ring decreased compared with the height in Fig. 6.8d, which indicates that ramified structures might be formed by particles in the ring and the particles in near the edge

due to the height decrease of the edge. The deposit is not radially symmetrical because of the change of the shape of peripheral ring.

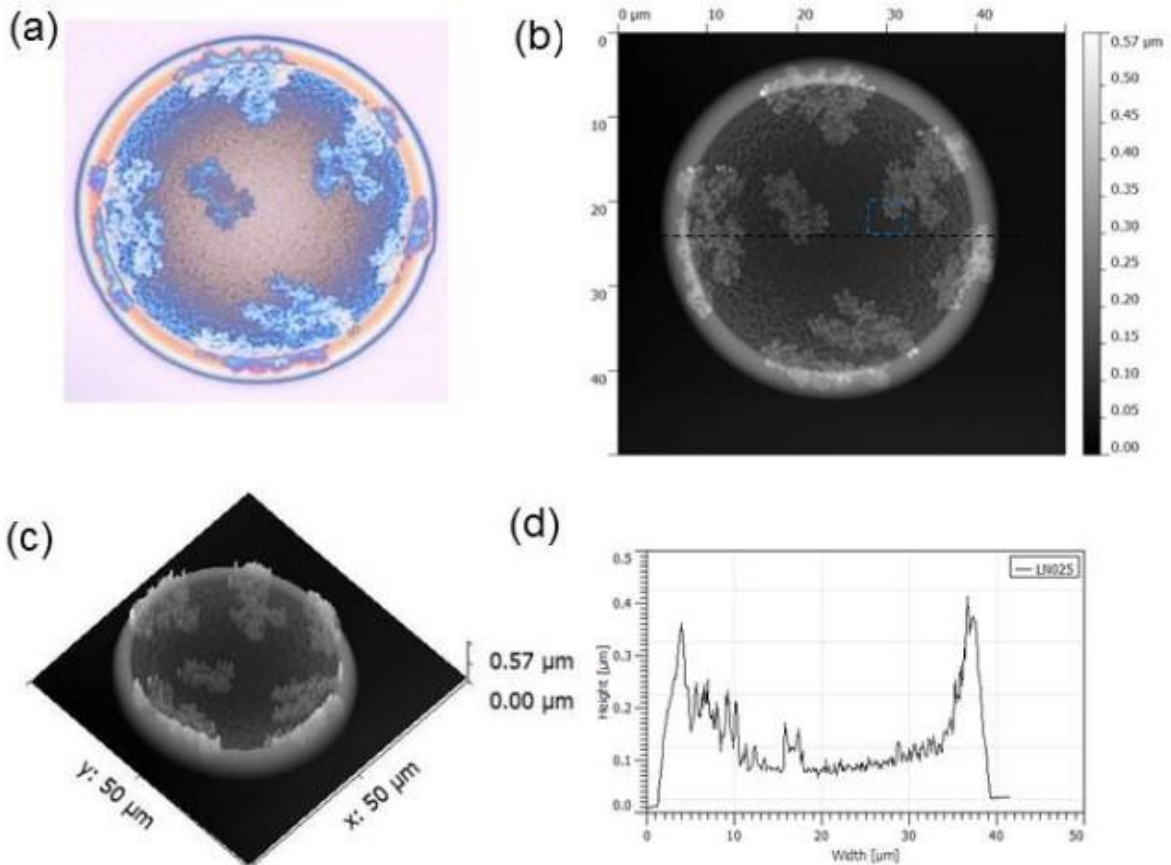


Figure 6.10. a) b) c) d) represent the same deposit one week after the sample (LN025) is made.

6.1.6 LN050

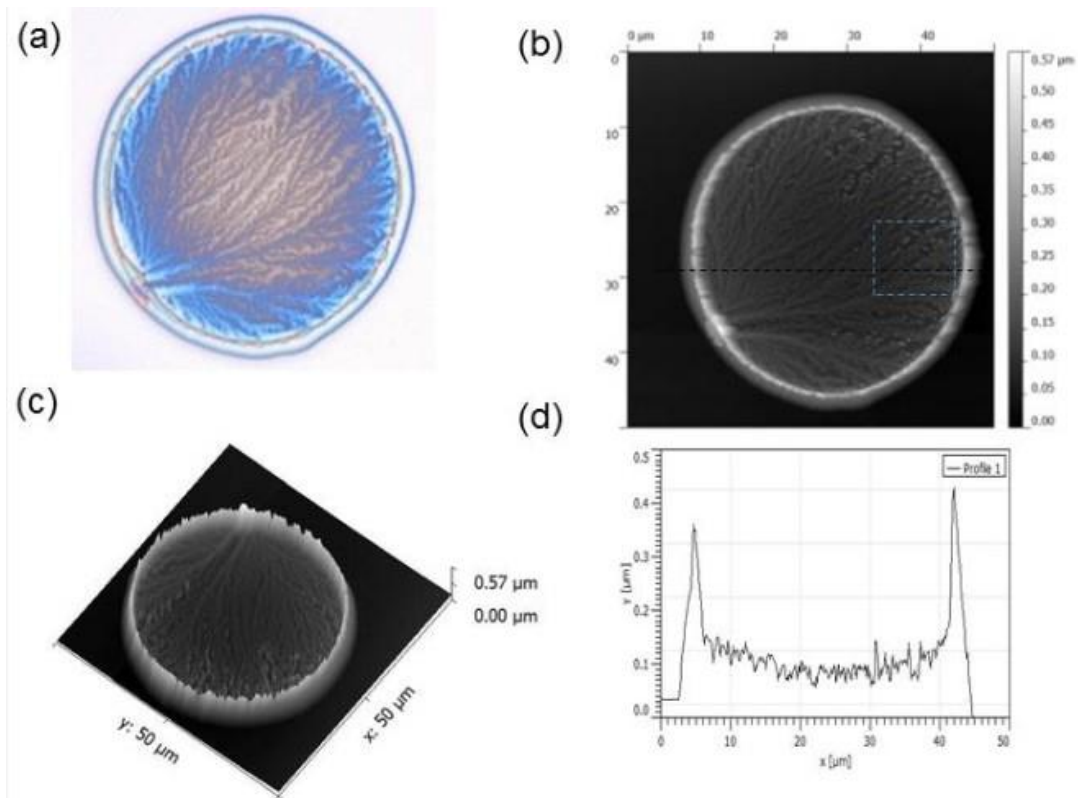


Figure 6.11. Representative images of a lysozyme-based drop deposit containing 0.50wt% NaCl. a) Optical microscopy image; b) 2-D view AFM topographic map (50µm X 50µm); c) 3-D view of AFM topography data; d) Cross-sectional height profile.

Figure 6.11 (a) and (b) optical image and AFM image, respectively, of lysozyme-based deposit containing 0.5 wt% NaCl, were obtained the day the sample was made. Figure 6.11d shows that the surface of the deposit is quite rough and the obvious peripheral ring is relatively sharp and narrow. Similar to the deposit containing 0.25 wt% NaCl, the central region has a shallow bowl shape with a minimum height at the very center. Branching dendritic forms grow across the deposit from an apparent nucleation point at roughly the 8 o'clock position at the periphery. These general features are observed in other deposits in the same sample. In deposits containing

0.5 wt% NaCl large crystals at the periphery of the ring appear to act as the origin from which dendritic structures grow. Occasionally, two source crystals are found in one deposit and dendrites grow from the two origins.

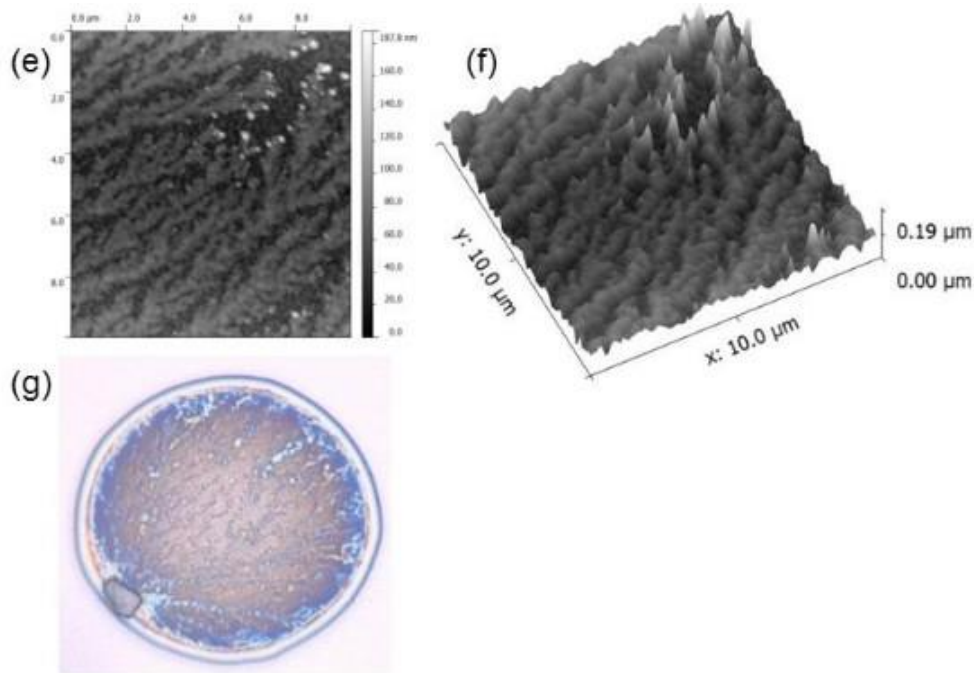


Figure 6.12. Detailed view of deposit interior indicated by the blue square in figure 6.12 (b), AFM topographic map (10µm X 10µm); f) 3-D view of AFM topography data, (10µm X 10µm); g) Optical image of the same deposit one week after the sample is made.

Figure 6.12(e) is a more detailed image from a region near the edge (marked with a blue square in Fig.6.11 (b) which shows that secondary and tertiary dendrite arms grow from the primary branches. The small cube shaped crystals found at the end of these branches are likely to be NaCl crystals. Fig.6.12 (g) shows the same deposit after one week stored under ambient conditions. Obvious changes have occurred. The dendritic structure in Region II has clearly degraded. A pattern of small rounded discrete crystals have replaced the dendrites, leaving a ‘residual skeleton’ of the former dendritic structure. The crystals acting as the nucleation point for the

original dendrites have grown substantially in just one week making it difficult to obtain clear AFM images. The average value of w/D is 0.081 and h_r/h_c is 3.48.

6.1.7 LN100

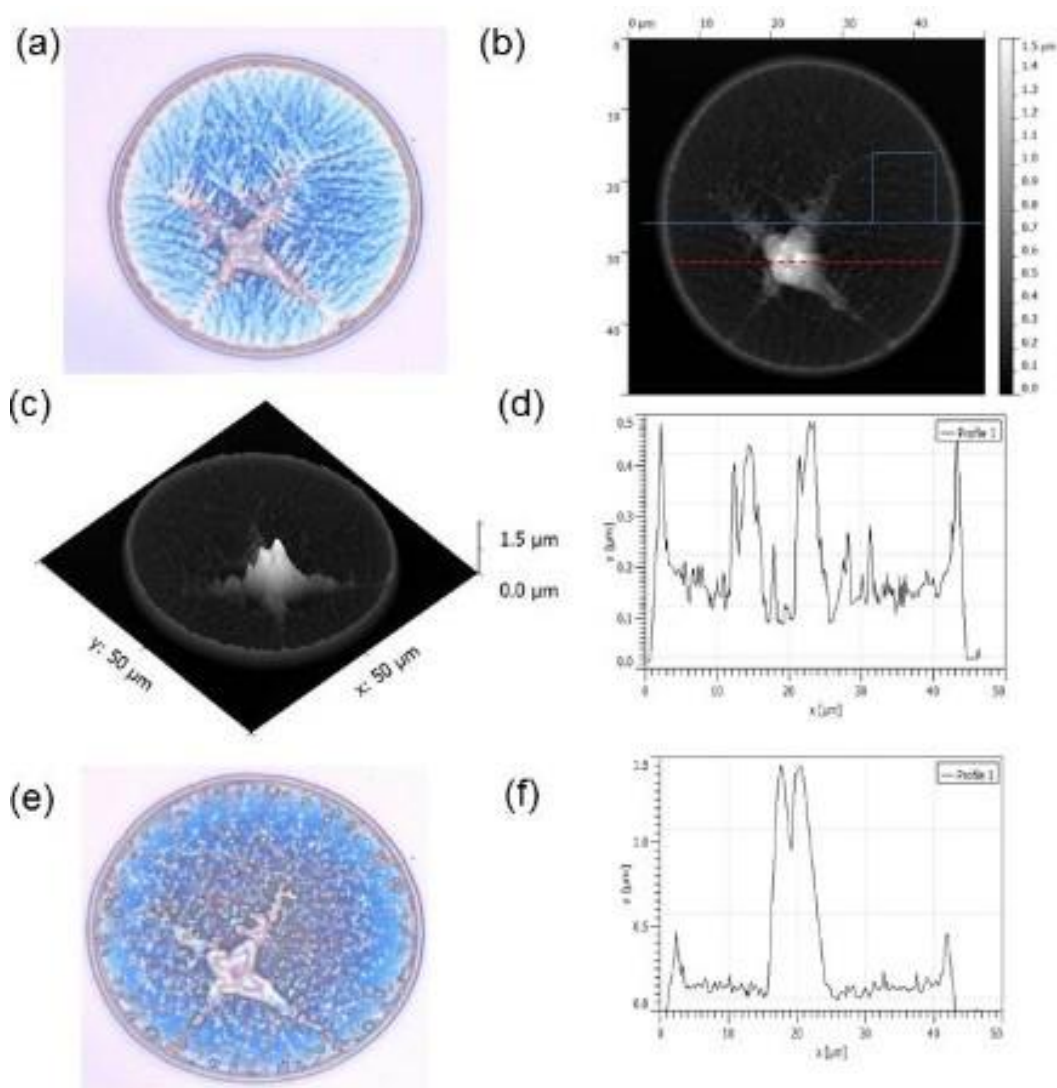


Figure 6.13. Representative images of a lysozyme-based drop deposit containing 1.0 wt% NaCl. a), e) Optical microscopy images; b) 2-D view AFM topographic map (50µm X 50µm); c) 3-D view of AFM topography data, (50µm X 50µm); d) Cross-sectional height profile through the center. (blue line in (b)); f) Central crystal height profile (marked with the red line in (b)).

Figure 6.13 (a) and (b) are optical and AFM images of a deposit containing 1 wt% NaCl taken on the day the sample was made. In the central region of the deposit, a large crystal with unusual concave faceting at its upper surface is observed. Four main dendritic branches at 90 degrees to one another grow from the central crystal. The central crystal is actually much higher than the height of peripheral ring. The concave faceting is displayed in the profile image (Fig.6.13f), which is a section (red line in Fig.6.13b) taken through the center of the large crystal. The concave angle of central crystal is $\sim 160^\circ$ (this is an average value calculated from similar crystals in eight deposits).

Compared with deposits containing 0.5 wt% NaCl, deposits containing 1 wt% NaCl are rougher in the central region. Figure 6.13 (e) shows the same deposit after one week stored under ambient conditions. Similar to the deposit containing 0.5 wt%, the dendritic structure clearly breaks up although the peripheral ring remains. The average value of w/D is 0.066. The value of h_r/h_c is not provided due to the large deviation among the chosen cross-sections.

6.2 AVERAGE VALUES OF w/D AND H_r/H_c

Table 6.1 documents the average value of w/D and H_r/H_c of deposits of various concentrations. The average value of w/D increases between pure lysozyme aqueous deposit and the deposit containing 0.01wt% NaCl, the maximum w/D is 0.34 which indicates that the ring of deposits containing 0.01wt% is wider than other deposits. Then, the value decreases from the deposit containing 0.01wt% NaCl to the deposit containing 1wt% NaCl, which shows that with the increase of NaCl in the 1wt% lysozyme solution, the ring width decreases.

Table 6.1. Average values of w/D and h_r/h_c

Sample	Average value of w/D	h_r/h_c
L100	0.26	2.3
LN001	0.34	1.6
LN005	0.16	3.0
LN010	-	-
LN025	0.11	2.7
LN050	0.08	3.5
LN100	0.07	-

6.3 EFFECT OF SALT CONCENTRATION ON PATTERN FORMATION

Sodium chloride ions strongly influence pattern formation in aqueous lysozyme solution colloidal drops. In a colloidal deposit without NaCl, a simple symmetric “coffee ring” was the most typical structure we obtained. When increasing amounts of NaCl are added to protein solutions, unique structures and geometries such as pore-like features, strip structures, dendrites, and large salt crystals are found in the dried deposits. For a given fixed lysozyme concentration of 1g/100ml, large salt crystals and dendrites were found in the deposits at the highest NaCl concentration. When the salt concentration is decreased to 0.25 wt%, instead of forming dendrites, small salt crystals and grainy aggregating were observed near the peripheral ring. At even lower NaCl concentration, the deposits may form a porous structure on the peripheral ring and a comparatively rough central region compared to deposits without NaCl. In this section,

more details about the morphology of the complex structures and illustrations of the mechanism of pattern formation are provided and analyzed.

6.3.1 The morphology of ring of deposits

Previous studies have documented the typical “coffee ring” structure in a drying sessile droplet. When a colloidal droplet is pinned at its contact line, solutes are driven to the contact line and aggregate in a peripheral ring. In our experiment, the “coffee ring” is greatly influenced by NaCl concentrations. An obvious trend in these observations is that as the salt concentration increases, the peripheral ring width decreases. The width of the ring is characterized by the value of w/D . The average value of w/D represents the relative ring size of each deposit and the relative salt concentration, ϕ_N , is the molar amount of salt divided by the molar amount of lysozyme. The dependence of w/D on ϕ_N is illustrated Figure 6.14 in the form $-\ln w/D$ vs $\ln \phi_N$. The best fit of the curve has a slope of 0.34 (1/3) and an R square value is 0.96. With this linear function, the width of the ring can be predicted: $y = 0.34x + 0.87$, $R^2 = 0.96$).

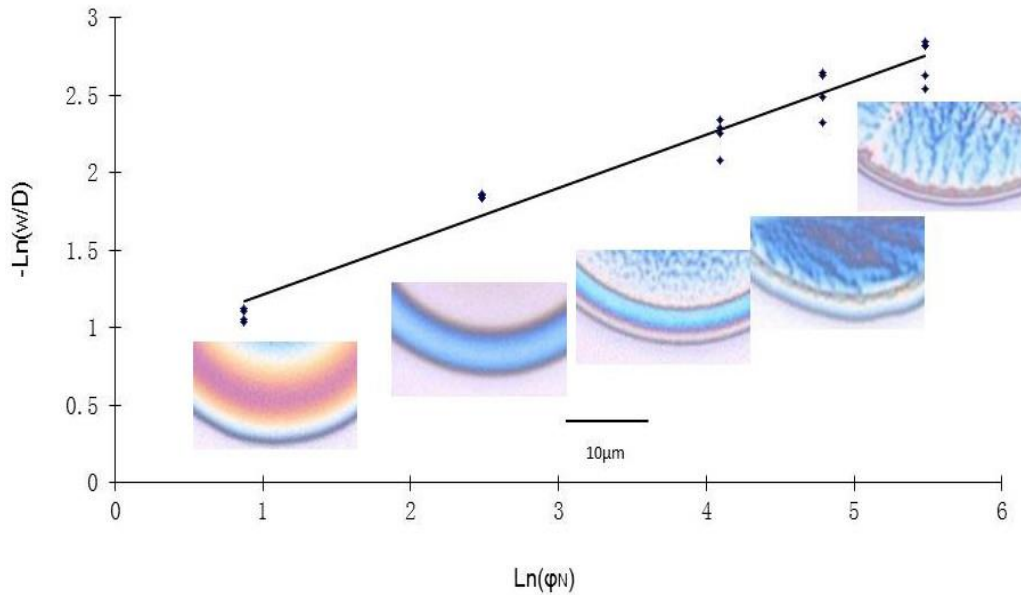


Figure 6.14. Plot of $-\ln(w/D)$ (relative width of Region I (ring)), vs. $\ln \phi_N$, the relative salt concentration. Inset in the graph are images showing Regions I for drops containing 0.01, 0.05, 0.25, 0.50, and 1.00 wt% NaCl.

The thickness of Region I does not exhibit as regular a behavior as the width. Generally as NaCl concentration increases, the thickness of peripheral ring decreases. However, there are larger deviations from the simple trend in h_r/h_c , especially for concentrations 0.05 wt% and 0.25 wt%.

6.3.2 Dendrites in the deposits of LN050 and LN100

Ferning patterns have been observed in human tear fluid, female cervical mucus and saliva. Pearce and Tomlinson [12] studied the components of tear ferning by using scanning electron microscopy, which showed that ferning patterns are formed by electrolytes such as Na, K and Cl rather than macromolecules. In our experiment, ferning patterns were found in micro-scaled deposits containing 0.5% and 1% NaCl. The details of the ferning structures are documented in figure 6.15. Both of the dendritic structures consist of main branches, secondary short branches

and even tertiary branches. Figure 6.15 (a) shows the dendritic structure of deposits containing 0.5wt % NaCl in which the branches of dendrites are thin and short compared with the branches in the figure 6.15 (b) which represents the structure of a deposit containing 1% NaCl. Also, the volume of branches in the deposit containing 1% NaCl is larger than that in figure (a).

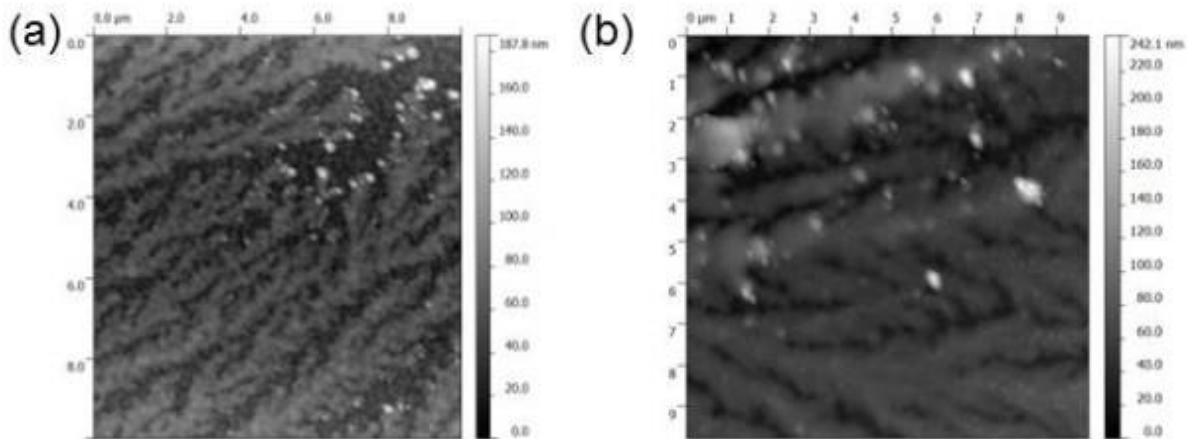


Figure 6.15. Detail images taken from deposits containing (a) 0.5% NaCl (b) 1% NaCl, AFM topographic map (10 μ m X 10 μ m).

Dendritic growth is a nonequilibrium growth of crystals from supersaturated solution. Studies [19] have focused on several requirements for dendritic growth, including thermodynamic flux, kinetic phase transitions, impurity flux density and supersaturation. As the deposit evaporates, different phases are created when the solution of deposit reaches a supersaturated concentration, then dendritic growth is repelled by the moving crystal surface until the supersaturated solution decreases to a certain concentration.

Also, impurities in the protein-salt solution affect the crystal nucleation and growth process in the micro-system. Local obstacles from nucleation are created and help to develop the branches. The sequence of the structure is formed by an increasing relative concentration of impurity which also influences the growth of secondary and tertiary branches. By an increasing

space of interbranch where impurity content spreads and more moveable, the density of dendritic structures decreases and might lead to tertiary branches. At the very ends of branches of both images, bright spots could be observed which represent the salt crystals where the viscosities of the solutions are much higher than the beginnings of branches leading to the ends of branches.

6.3.3 Pore-like structures on the rings

In our experiment, pore-like structures are another obvious feature found on the rings in deposits containing 0.05wt % and 0.25wt % NaCl; these are documented in figure 6.16.

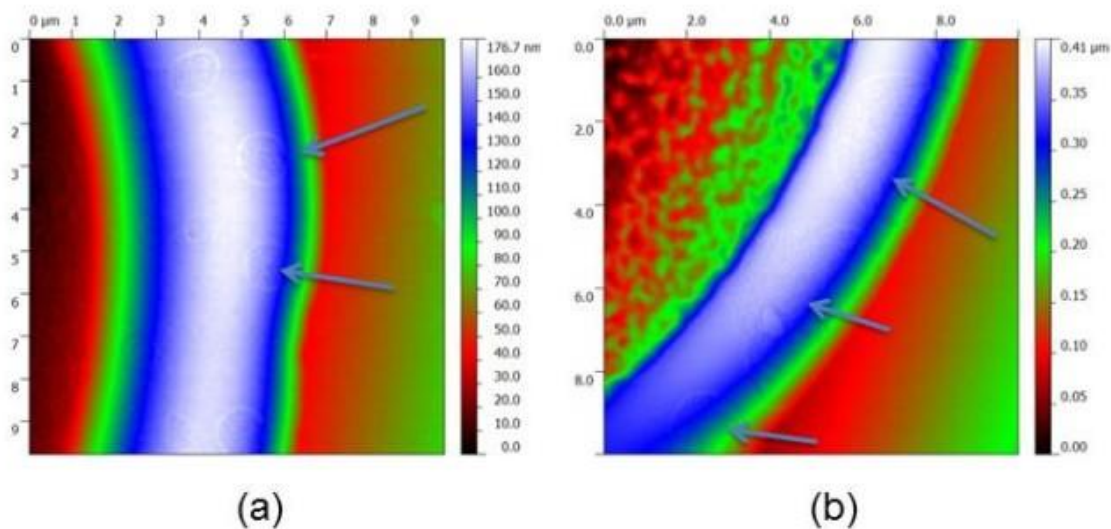


Figure 6.16.Detail images taken from deposits containing (a) 0.05% NaCl (b) 0.25% NaCl, AFM topographic map (10μm X 10μm)

Small circles were observed on the peripheral ring for deposits containing 0.05% NaCl while semicircles were found on the ring for deposits containing 0.25% NaCl. With increasing salt concentration, the pore-like structures become larger and then disappear when the salt concentration reaches 0.5%. The small circle or semicircle structures are combined with two regions: outer circles region and inner circle region. The inner circle region is rougher and grainy

which might be salt-rich phase. While the outer circle region is smooth and skinny, which might be a ring region covered with a gel phase formed by colloidal molecules. Surface tension caused by phase transition may play a role in forming the pore-like structures. The ring is sharper and its width is thinner when the concentration of NaCl increases as described above, and the surface tension of ring becomes higher, where the salt crystals domains.

Also, even though the surface of the deposit containing 0.01% NaCl looks smooth and only a few salt crystals can be seen in the AFM image, our SEM analysis shows that small salt crystalline aggregates and tiny pore structures are scattered throughout region III. A reasonable assumption is that when the final liquid evaporates from the gel phase, porous structures were created as the liquid percolates. Additionally, the salt crystalline aggregates are on the top of the surface.

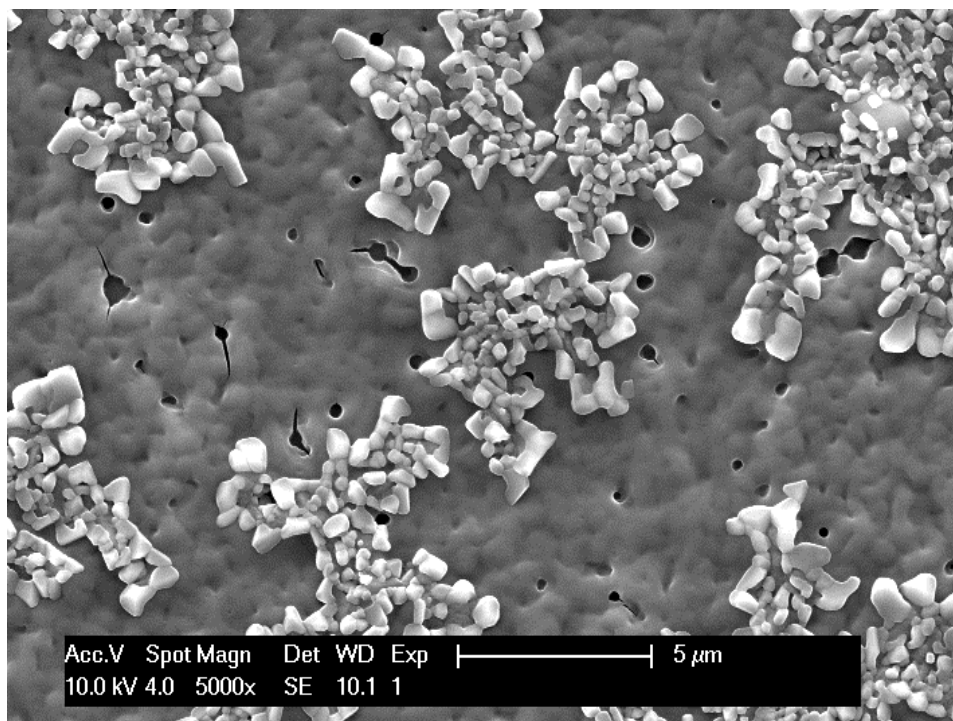


Figure 6.17. SEM image of the central region (Region III) of a lysozyme-based deposit containing 0.01 wt%

NaCl[37].

7.0 CONCLUSION

This thesis provides insight into the morphologic of the features which develop during evaporation of micro-scale drops of aqueous lysozyme and NaCl solutions. This solution is used as a simple model of a biofluid. Aqueous lysozyme – NaCl solutions are shown to leave variable dried patterns that can be correlated with small changes in solution chemistry. These patterns may be used to develop a reference library of images that can then be studied with image analysis techniques. Sample of unknown chemistry may then be categorized using image recognition techniques. The key conclusions of this thesis are organized in three parts: morphology of the dried residue in the deposit, the topography of the deposits and time dependence.

7.1 MORPHOLOGICAL PATTERNS

With increasing concentration of NaCl in the drop, the surface of the deposits becomes rougher until crystals emerge in the deposits at a NaCl concentration higher than 0.25wt %. Pore-like structures are observed on the peripheral rings in the deposits with NaCl concentrations from 0.05wt% to 0.25 wt%. In the deposits with a low salt concentration of 0.10wt%, pore-like structures cover the whole surface. In the deposits with a NaCl concentration of 0.25wt%,

aggregated small crystalline grains may form a transition region with a high density of crystals or a large crystal group may form. Both forms are observed in deposits with this concentration.

When the NaCl concentration increases to 0.5wt%, dendrites grow from large crystals which may be located either in the central region or near the ring and spread radially towards the ring region. These dendrites are thin and their secondary or tertiary branches are short compared with the same structures in the deposits containing higher salt concentration. In the deposits containing 1wt% NaCl, cross-like dendrites form from a main crystal in the central region which has an unusual concave angle of $\sim 160^\circ$. Dendrites grow from the four main branches followed by secondary and tertiary branches.

7.2 TOPOGRAPHICAL FEATURES

With the basic aqueous 1wt% lysozyme solution (no salt), the lysozyme deposit shows a peripheral ring and a slight mound in the central region with a small dip in the very center (note that the dip structure is not found in any of the lysozyme-NaCl deposits). The central mound region is still observed in the deposits containing 0.01wt% NaCl. Also, for the deposits containing 0.01wt% NaCl, the relative width of the ring is wider than the pure lysozyme deposits. Beyond this NaCl concentration the relative width of the ring region decreases.

Central region depression is a phenomenon that emerges in deposits containing 0.10wt%, 0.25wt% and 0.50wt% NaCl. For these deposits, the thickness at the center decreases to a minimum and rises gradually to the ring region. In addition, two patterns are found for the

deposits containing 0.10wt% NaCl, one has a central bump and the other is a central depression although neither of them have peripheral rings.

7.3 TIME DEPENDENCE

The patterns observed in our experiments show a difference in stability with solution chemistry. For the deposits with low NaCl concentrations (less than 0.10 g/100ml), their patterns are stable monitored over two months. For the deposits with a NaCl concentration of 0.25g/100ml, crystalline aggregates grow in the pattern within a week and the new pattern is stable during the rest of the monitoring time. For the deposits with higher NaCl concentrations (higher than 0.5g/ml), the dendritic crystals in these patterns can change within two or three days. Basically, the ferning structures formed by salt crystals become disconnected with time. With increasing time, large crystals take the place of the dendritic structures.

Despite the lack of a detailed insight into the explanation of mechanisms the formation of these patterns, this project highlights morphologies of the micro-scale drops with various lysozyme-NaCl solutions and establishes the feasibility of computer-based disease detection methods. Similar programs already exist based on iris scans for person identification. Thus, it seems very possible that such a method can and will be developed for cost-effective and early detection of diseases. Further investigation could focus on developing computer programs to achieve the recognition match system based on an image database. Also, by adding various components to the biofluids to amplify the research databases, the works can be more focused on medical and clinical detection.

BIBLIOGRAPHY

- [1] R. D. Deegan, O. Bakajin, T. F. Dupont, G. Huber, S. R. Nagel, and T. A. Witten, “Capillary flow as the cause of ring stains from dried liquid drops,” *Nature*, vol. 389, no. 6653, pp. 827–829, Oct. 1997.
- [2] D. Brutin, B. Sobac, B. Loquet, and J. Sampaol, “Pattern formation in drying drops of blood,” *Journal of Fluid Mechanics*, vol. 667, pp. 85–95, Jan. 2011.
- [3] R. Bhardwaj, X. Fang, and D. Attinger, “Pattern formation during the evaporation of a colloidal nanoliter drop: a numerical and experimental study,” *New Journal of Physics*, vol. 11, p. 075020, 2009.
- [4] L. Pauchard and C. Allain, “Stable and unstable surface evolution during the drying of a polymer solution drop,” *Physical Review E*, vol. 68, no. 5, Nov. 2003.
- [5] Y. Y. Tarasevich, I. V. Vodolazskaya, and O. P. Isakova, “Desiccating colloidal sessile drop: dynamics of shape and concentration,” *Colloid and Polymer Science*, vol. 289, no. 9, pp. 1015–1023, Apr. 2011.
- [6] P. G. de Gennes, “Solvent evaporation of spin cast films: ‘crust’ effects,” *The European Physical Journal E: Soft Matter and Biological Physics*, vol. 7, no. 1, pp. 31–34, 2002.
- [7] P. Takhistov and H.-C. Chang, “Complex stain morphologies,” *Industrial & engineering chemistry research*, vol. 41, no. 25, pp. 6256–6269.
- [8] I. I. Smalyukh, O. V. Zribi, J. C. Butler, O. D. Lavrentovich, and G. C. L. Wong, “Structure and Dynamics of Liquid Crystalline Pattern Formation in Drying Droplets of DNA,” *Phys. Rev. Lett.*, vol. 96, no. 17, p. 177801, May 2006.
- [9] J. Xu and D. Attinger, “Drop on demand in a microfluidic chip,” *Journal of Micromechanics and Microengineering*, vol. 18, no. 6, p. 065020, Jun. 2008.
- [10] K. A. Esmonde-White, G. S. Mandair, F. W. L. Esmonde-White, F. Raaii, B. J. Roessler, and M. D. Morris, “Osteoarthritis screening using Raman spectroscopy of dried human synovial fluid drops,” 2009, p. 71660J–71660J–8.

- [11] J. Filik and N. Stone, "Analysis of human tear fluid by Raman spectroscopy," *Analytica Chimica Acta*, vol. 616, no. 2, pp. 177–184, Jun. 2008.
- [12] E. Pearce, "Spatial location studies on the chemical composition of human tear ferns," *Ophthalmic and Physiological Optics*, vol. 20, no. 4, pp. 306–313, Jun. 2000.
- [13] H. M. Gorr, J. M. Zueger, and J. A. Barnard, "Lysozyme Pattern Formation in Evaporating Drops," *Langmuir*, vol. 28, no. 9, pp. 4039–4042, Mar. 2012.
- [14] D. Ronen, E. Eylan, A. Romano, R. Stein, and M. Modan, "A spectrophotometric method for quantitative determination of lysozyme in human tears: description and evaluation of the method and screening of 60 healthy subjects.," *IOVS*, vol. 14, no. 6, pp. 479–484, Jun. 1975.
- [15] C. K. Yeh, M. W. Dodds, P. Zuo, and D. A. Johnson, "A population-based study of salivary lysozyme concentrations and candidal counts," *Arch. Oral Biol.*, vol. 42, no. 1, pp. 25–31, Jan. 1997.
- [16] T. Young, "An Essay on the Cohesion of Fluids," *Phil. Trans. R. Soc. Lond.*, vol. 95, pp. 65–87, Jan. 1805.
- [17] R. D. Deegan, "Pattern formation in drying drops," *Physical Review E*, vol. 61, no. 1, p. 475, 2000.
- [18] R. D. Deegan, O. Bakajin, T. F. Dupont, G. Huber, S. R. Nagel, and T. A. Witten, "Contact line deposits in an evaporating drop," *Physical Review E*, vol. 62, no. 1, pp. 756–765, 2000.
- [19] Sommer, A. P. Limits of the Impact of Gravity on Self-Organizing Nanospheres. *The Journal of Physical Chemistry B* 108, 8096–8098 (2004).
- [20] H. Hu and R. G. Larson, "Analysis of the Effects of Marangoni Stresses on the Microflow in an Evaporating Sessile Droplet," *Langmuir*, vol. 21, no. 9, pp. 3972–3980, Apr. 2005.
- [21] H. Hu and R. G. Larson, "Analysis of the Microfluid Flow in an Evaporating Sessile Droplet," *Langmuir*, vol. 21, no. 9, pp. 3963–3971, Apr. 2005.
- [22] A. S. Dimitrov, C. D. Dushkin, H. Yoshimura, and K. Nagayama, "Observations of Latex Particle Two-Dimensional-Crystal Nucleation in Wetting Films on Mercury, Glass, and Mica," *Langmuir*, vol. 10, no. 2, pp. 432–440, Feb. 1994.
- [23] A. P. Sommer, "Limits of the Impact of Gravity on Self-Organizing Nanospheres," *The Journal of Physical Chemistry B*, vol. 108, no. 24, pp. 8096–8098, Jun. 2004.
- [24] H. Wei, Z. Wang, J. Zhang, S. House, Y.-G. Gao, L. Yang, H. Robinson, L. H. Tan, H. Xing, C. Hou, I. M. Robertson, J.-M. Zuo, and Y. Lu, "Time-dependent, protein-directed

- growth of gold nanoparticles within a single crystal of lysozyme,” *Nature Nanotechnology*, vol. 6, no. 2, pp. 93–97, Jan. 2011.
- [25] A. A. Vertegel, R. W. Siegel, and J. S. Dordick, “Silica Nanoparticle Size Influences the Structure and Enzymatic Activity of Adsorbed Lysozyme,” *Langmuir*, vol. 20, no. 16, pp. 6800–6807, Aug. 2004.
- [26] L. Huang, X. Cui, G. Dukovic, and S. P. O'Brien, “Self-organizing high-density single-walled carbon nanotube arrays from surfactant suspensions,” *Nanotechnology*, vol. 15, no. 11, pp. 1450–1454, Nov. 2004.
- [27] H. Ko, S. Peleshanko, and V. V. Tsukruk, “Combing and Bending of Carbon Nanotube Arrays with Confined Microfluidic Flow on Patterned Surfaces,” *The Journal of Physical Chemistry B*, vol. 108, no. 14, pp. 4385–4393, Apr. 2004.
- [28] R. Duggal, F. Hussain, and M. Pasquali, “Self-Assembly of Single-Walled Carbon Nanotubes into a Sheet by Drop Drying,” *Advanced Materials*, vol. 18, no. 1, pp. 29–34, Jan. 2006.
- [29] J.-U. Park, M. A. Meitl, S.-H. Hur, M. L. Usrey, M. S. Strano, P. J. A. Kenis, and J. A. Rogers, “In Situ Deposition and Patterning of Single-Walled Carbon Nanotubes by Laminar Flow and Controlled Flocculation in Microfluidic Channels,” *Angewandte Chemie International Edition*, vol. 45, no. 4, pp. 581–585, Jan. 2006.
- [30] B. Sobac and D. Brutin, “Structural and evaporative evolutions in desiccating sessile drops of blood,” *Physical Review E*, vol. 84, no. 1, Jul. 2011.
- [31] C. C. Annarelli, J. Fornazero, J. Bert, and J. Colombani, “Crack patterns in drying protein solution drops,” *The European Physical Journal E: Soft Matter and Biological Physics*, vol. 5, no. 5, pp. 599–603, 2001.
- [32] A. Accardo, F. Gentile, F. Mecarini, F. De Angelis, M. Burghammer, E. Di Fabrizio, and C. Riekkel, “In Situ X-ray Scattering Studies of Protein Solution Droplets Drying on Micro- and Nanopatterned Superhydrophobic PMMA Surfaces,” *Langmuir*, vol. 26, no. 18, pp. 15057–15064, Sep. 2010.
- [33] N. Kumar, K. Varanasi, R. D. Tilton, and S. Garoff, “Surfactant Self-Assembly ahead of the Contact Line on a Hydrophobic Surface and Its Implications for Wetting,” *Langmuir*, vol. 19, no. 13, pp. 5366–5373, Jun. 2003.
- [34] S. P. Rozhkov and A. S. Goryunov, “Thermodynamic study of protein phases formation and clustering in model water–protein–salt solutions,” *Biophysical Chemistry*, vol. 151, no. 1–2, pp. 22–28, Sep. 2010.
- [35] M. Fritz, M. Radmacher, J. P. Cleveland, M. W. Allersma, R. J. Stewart, R. Gieselmann, P. Janmey, C. F. Schmidt, and P. K. Hansma, “Imaging Globular and Filamentous

- Proteins in Physiological Buffer Solutions with Tapping Mode Atomic Force Microscopy,” *Langmuir*, vol. 11, no. 9, pp. 3529–3535, Sep. 1995.
- [36] Y. Xie, J. Zhou, and S. Jiang, “Parallel tempering Monte Carlo simulations of lysozyme orientation on charged surfaces,” *The Journal of Chemical Physics*, vol. 132, no. 6, p. 065101, 2010.
- [37] H. M. Gorr, J. M. Zueger, D. R. McAdams, and J. A. Barnard, “Salt-induced pattern formation in evaporating droplets of lysozyme solutions,” *Colloids Surf B Biointerfaces*, vol. 103, pp. 59–66, Mar. 2013.
- [38] X. Shen, C.-M. Ho, and T.-S. Wong, “Minimal Size of Coffee Ring Structure,” *The Journal of Physical Chemistry B*, vol. 114, no. 16, pp. 5269–5274, Apr. 2010.
- [39] M. T. Kuo, C. C. Lin, H. Y. Liu, and H. C. Chang, “Tear Analytical Model Based on Raman Microspectroscopy for Investigation of Infectious Diseases of the Ocular Surface,” *Investigative Ophthalmology & Visual Science*, vol. 52, no. 7, pp. 4942–4950, 2011.
- [40] V. Ng and P. Cho, “The relationship between total tear protein concentrations determined by different methods and standards,” *Graefe’s archive for clinical and experimental ophthalmology*, vol. 238, no. 7, pp. 571–576, 2000.
- [41] M. A. Lieberman and A. Marks, *Marks’ Basic Medical Biochemistry: A Clinical Approach*. Lippincott Williams & Wilkins, 2008.
- [42] S. N. S. V N Shabalina, “Diagnostic markers in the structures of human biological liquids,” *Singapore medical journal*, vol. 48, no. 5, pp. 440–6, 2007.
- [43] T. A. Yakhno, V. G. Yakhno, A. G. Sanin, O. A. Sanina, A. S. Pelyushenko, N. A. Egorova, I. G. Terentiev, S. V. Smetanina, O. V. Korochkina, and E. V. Yashukova, “The informative-capacity phenomenon of drying drops,” *Engineering in Medicine and Biology Magazine, IEEE*, vol. 24, no. 2, pp. 96–104, 2005.
- [44] R. Sariri and H. Ghafoori, “Tear proteins in health, disease, and contact lens wear,” *Biochemistry (Moscow)*, vol. 73, no. 4, pp. 381–392, May 2008.
- [45] Y. Jia, J. Narayanan, X.-Y. Liu, and Y. Liu, “Investigation on the Mechanism of Crystallization of Soluble Protein in the Presence of Nonionic Surfactant,” *Biophysical Journal*, vol. 89, no. 6, pp. 4245–4251, Dec. 2005.
- [46] M. L. Pusey, R. S. Snyder, and R. Naumann, “Protein crystal growth. Growth kinetics for tetragonal lysozyme crystals,” *Journal of Biological Chemistry*, vol. 261, no. 14, pp. 6524–6529, 1986.
- [47] P. Umbach, Y. Georgalis, and W. Saenger, “Time-resolved small-angle static light scattering on lysozyme during nucleation and growth,” *Journal of the American Chemical Society*, vol. 120, no. 10, pp. 2382–2390, 1998.

- [48] J. G. Albright, O. Annunziata, D. G. Miller, L. Paduano, and A. J. Pearlstein, "Precision Measurements of Binary and Multicomponent Diffusion Coefficients in Protein Solutions Relevant to Crystal Growth: Lysozyme Chloride in Water and Aqueous NaCl at pH 4.5 and 25 °C". *Journal of the American Chemical Society*, vol. 121, no. 14, pp. 3256 – 3266, Apr. 1999.
- [49] S. M. Daly, T. M. Przybycien, and R. D. Tilton, "Adsorption of Poly(ethylene glycol)-Modified Lysozyme to Silica," *Langmuir*, vol. 21, no. 4, pp. 1328–1337, Feb. 2005.
- [50] R. D. Tilton, E. Blomberg, and P. M. Claesson, "Effect of anionic surfactant on interactions between lysozyme layers adsorbed on mica," *Langmuir*, vol. 9, no. 8, pp. 2102–2108, 1993.
- [51] D. T. Kim, H. W. Blanch, and C. J. Radke, "Direct Imaging of Lysozyme Adsorption onto Mica by Atomic Force Microscopy," *Langmuir*, vol. 18, no. 15, pp. 5841–5850, Jul. 2002.
- [52] M. Radmacher, M. Fritz, J. P. Cleveland, D. A. Walters, and P. K. Hansma, "Imaging adhesion forces and elasticity of lysozyme adsorbed on mica with the atomic force microscope," *Langmuir*, vol. 10, no. 10, pp. 3809–3814, Oct. 1994.
- [53] M. Boström, F. W. Tavares, S. Finet, F. Skouri-Panet, A. Tardieu, and B. W. Ninham, "Why forces between proteins follow different Hofmeister series for pH above and below pI," *Biophys. Chem.*, vol. 117, no. 3, pp. 217–224, Oct. 2005.
- [54] C. C. F. Blake, D. F. Koenig, G. A. Mair, A. C. T. North, D. C. Phillips, and V. R. Sarma, "Structure of Hen Egg-White Lysozyme: A Three-dimensional Fourier Synthesis at 2 [ångström] Resolution," , Published online: 22 May 1965; | doi:10.1038/206757a0, vol. 206, no. 4986, pp. 757–761, May 1965.
- [55] F. Leisten, M. Wiechmann, O. Enders, and H.-A. Kolb, "Generation of nanostructures of mica supported lysozyme molecules in aqueous solution by atomic force microscopy," *Journal of Colloid and Interface Science*, vol. 298, no. 2, pp. 508–514, Jun. 2006.
- [56] D. E. Kuehner, J. Engmann, F. Fergg, M. Wernick, H. W. Blanch, and J. M. Prausnitz, "Lysozyme Net Charge and Ion Binding in Concentrated Aqueous Electrolyte Solutions," *The Journal of Physical Chemistry B*, vol. 103, no. 8, pp. 1368–1374, Feb. 1999.
- [57] I. V. Nesmelova, V. D. Skirda, and V. D. Fedotov, "Generalized concentration dependence of globular protein self-diffusion coefficients in aqueous solutions," *Biopolymers*, vol. 63, no. 2, pp. 132–140, Feb. 2002.
- [58] G. C. Fadda and D. Lairez, "Evidence for a rigid structure in lysozyme fractal aggregates," *Physica A: Statistical Mechanics and its Applications*, vol. 304, no. 1–2, pp. 271–275, Feb. 2002.

- [59] W. S. Price, F. Tsuchiya, and Y. Arata, "Lysozyme Aggregation and Solution Properties Studied Using PGSE NMR Diffusion Measurements," *Journal of the American Chemical Society*, vol. 121, no. 49, pp. 11503–11512, Dec. 1999.
- [60] S. Fermani, G. Falini, M. Minnucci, and A. Ripamonti, "Protein crystallization on polymeric film surfaces," *Journal of crystal growth*, vol. 224, no. 3, pp. 327–334, 2001.
- [61] R. A. Judge, R. S. Jacobs, T. Frazier, E. H. Snell, and M. L. Pusey, "The effect of temperature and solution pH on the nucleation of tetragonal lysozyme crystals," *Biophysical journal*, vol. 77, no. 3, pp. 1585–1593, 1999.
- [62] L. M. Martyushev, V. D. Seleznev, and S. A. Skopinov, "Reentrant kinetic phase transitions during dendritic growth of crystals in a two-dimensional medium with phase separation," *Technical Physics Letters*, vol. 23, no. 7, pp. 495–497, 1997.
- [63] Y. Liu, X. Wang, and C. B. Ching, "Toward Further Understanding of Lysozyme Crystallization: Phase Diagram, Protein–Protein Interaction, Nucleation Kinetics, and Growth Kinetics," *Crystal Growth & Design*, vol. 10, no. 2, pp. 548–558, Feb. 2010.
- [64] M. Muschol and F. Rosenberger, "Liquid–liquid phase separation in supersaturated lysozyme solutions and associated precipitate formation/crystallization," *The Journal of Chemical Physics*, vol. 107, no. 6, p. 1953, 1997.
- [65] F. Cardinaux, T. Gibaud, A. Stradner, and P. Schurtenberger, "Interplay between Spinodal Decomposition and Glass Formation in Proteins Exhibiting Short-Range Attractions," *Physical Review Letters*, vol. 99, no. 11, Sep. 2007.
- [66] P. Segrè, V. Prasad, A. Schofield, and D. Weitz, "Glasslike Kinetic Arrest at the Colloidal-Gelation Transition," *Physical Review Letters*, vol. 86, no. 26, pp. 6042–6045, Jun. 2001.
- [67] F. Cardinaux, A. Stradner, P. Schurtenberger, F. Sciortino, and E. Zaccarelli, "Modeling equilibrium clusters in lysozyme solutions," *Europhysics Letters (EPL)*, vol. 77, no. 4, p. 48004, Feb. 2007.
- [68] S. Sundaram, J. K. Ferri, D. Vollhardt, and K. J. Stebe, "Surface Phase Behavior and Surface Tension Evolution for Lysozyme Adsorption onto Clean Interfaces and into DPPC Monolayers: Theory and Experiment," *Langmuir*, vol. 14, no. 5, pp. 1208–1218, Mar. 1998.
- [69] P. J. Lu, E. Zaccarelli, F. Ciulla, A. B. Schofield, F. Sciortino, and D. A. Weitz, "Gelation of particles with short-range attraction," *Nature*, vol. 453, no. 7194, pp. 499–503, May 2008.
- [70] G. Chen and G. J. Mohamed, "Complex protein patterns formation via salt-induced self-assembly and droplet evaporation," *The European Physical Journal E*, vol. 33, no. 1, pp. 19–26, Sep. 2010.

- [71] D. Kaya, V. A. Belyi, and M. Muthukumar, "Pattern formation in drying droplets of polyelectrolyte and salt," *The Journal of Chemical Physics*, vol. 133, no. 11, pp. 114905–114905–9, Sep. 2010.